Dynamics of Near-Bottom Currents in Cold-Water Coral and Sponge Areas at Valdivia Bank and Ewing Seamount, Southeast Atlantic

Christian Mohn[1,2] , Franziska U. Schwarzkopf[3] , Patricia Jiménez García[4], Covadonga Orejas[2,5], Veerle A. I. Huvenne[2,6], Mia Schumacher[3], Irene Pérez-Rodríguez[7] , Roberto Sarralde Vizuete[7], Luis J. López-Abellán[8] , Andrew C. Dale[9] , Colin Devey[3] , Jørgen L. S. Hansen[1], Eva Friis Møller[1] , and Arne Biastoch[3,10]

[1]Department of Ecoscience, Aarhus University, Roskilde, Denmark, [2]Hanse-Wissenschaftskolleg—Institute for Advanced Study (HWK), Delmenhorst, Germany, [3]GEOMAR Helmholtz Centre for Ocean Research Kiel, Kiel, Germany, [4]Tragsatec, Balearic Islands, Spain, [5]Centro Oceanográfico de Gijón, Instituto Español de Oceanografía, IEO-CSIC, Gijón, Spain, [6]Ocean BioGeosciences, National Oceanography Centre, Southampton, UK, [7]Centro Oceanográfico de Vigo, Instituto Español de Oceanografía, IEO-CSIC, Vigo, Spain, [8]Centro Oceanográfico de Canarias, Instituto Español de Oceanografía, IEO-CSIC, Santa Cruz de Tenerife, Spain, [9]Scottish Association for Marine Science, Oban, UK, [10]Kiel University, Kiel, Germany

Abstract This study investigates near-bottom currents and physical processes from simulations with the hydrodynamic model ROMS-AGRIF at two seamounts of the northeast Walvis Ridge to obtain valuable insights about drivers of observed occurrences of benthic suspension feeders (cnidarians and sponges) in this data-poor area. The spatial resolution in each model area was increased across two levels of nested grids from 1,500 m to 500 m resolution with 32 stretched terrain-following (s-) layers in the vertical with high resolution close to the bottom. The parent grids receive initial and boundary conditions from the basin-scale model INALT20 and from solutions of the OTIS inverse tidal model. The model topography is based on GEBCO data with local refinements from multi-beam data collected during different surveys in 2008, 2009, and 2010. Increasing model resolution is an important advancement for precisely evaluating the intrinsic dynamics within challenging rough terrain. We examined how near-bottom currents vary over space and time and investigated potential links between observed Cnidarian and Porifera occurrences and ranges of physical variables and processes. We identified a close link between physical processes and species distributions and suggested that physical processes such as kinetic energy dissipation and internal wave dynamics may be considered in future research as proxies of food supply to benthic suspension feeders. Such mechanistic variables may also be used to supplement more traditional descriptors such as water mass and terrain properties in species distribution models, thus enhancing our ability to predict the occurrence of benthic communities characterized by cnidarians and sponges.

Plain Language Summary We investigated the physical drivers of the distribution of cnidarians and sponges in two areas along the northeast Walvis Ridge, Valdivia Bank, and Ewing Seamount based on data from ocean model simulations over a period of 3 years. To get realistic boundary conditions for our simulations, we added bathymetric data from high-resolution seafloor topography, water column data from a larger-scale ocean circulation model, and information about tidal currents. By refining our model, we were able to better resolve the near-bottom circulation and how it changes over time and space. Incorporating finer-scale variability of physical variables and processes that represent important proxies for the transport and delivery of food to deep-sea benthic fauna has the potential to greatly improve predictions of benthic filter feeding communities. Moreover, integration of such variables in future species distribution modeling may contribute to our current understanding of optimal environmental envelopes for important deep-sea taxa, such as those that represent vulnerable marine ecosystems.

1. Introduction

The global ocean seafloor is covered with countless isolated topographic elevations from smaller knolls and pinnacles only several hundred meters high to intermediate and large seamounts rising several thousand meters above the seafloor occasionally entering the photic zone (Gevorgian et al., 2023; Wessel et al., 2010). Despite the

Roberto Sarralde Vizuete, Luis J. López-Abellán, Andrew C. Dale, Jørgen L. S. Hansen, Eva Friis Møller
Methodology: Christian Mohn, Franziska U. Schwarzkopf, Covadonga Orejas, Veerle A. I. Huvenne, Mia Schumacher, Irene Pérez-Rodríguez, Roberto Sarralde Vizuete, Andrew C. Dale, Colin Devey, Jørgen L. S. Hansen, Eva Friis Møller, Arne Biastoch
Resources: Colin Devey
Software: Franziska U. Schwarzkopf, Arne Biastoch
Writing – original draft: Christian Mohn, Franziska U. Schwarzkopf, Covadonga Orejas, Veerle A. I. Huvenne, Irene Pérez-Rodríguez, Roberto Sarralde Vizuete, Andrew C. Dale
Writing – review & editing: Christian Mohn

widespread existence of seamounts, our understanding of the structure and functioning of seamount ecosystems remains remarkably limited as highlighted by Rogers (2018). A growing number of seamounts in the North Atlantic are systematically investigated across disciplines (Giacomello et al., 2013; Ramiro-Sánchez et al., 2019; Serrano et al., 2017; Simpson & Watling, 2011; Tojeira et al., 2023), but seamounts in the southeast Atlantic have received comparatively less attention, resulting in sparse or inadequately documented data regarding benthic communities, fish populations, and environmental water column characteristics (Bergstad, Gil, et al., 2019, Bergstad, Høines, et al., 2019). However, significant progress has been made in the South Atlantic in recent times. Notably, during the Spanish-Namibian collaborative effort RAP-SUR (2008–2010), spatially resolved data on geology, benthos, fish, seabirds, and water mass properties were collected at the summits of the Valdivia Bank and at Ewing Seamount (López-Abellán & Holtzhausen, 2011). In addition, Bergstad, Gil, et al. (2019) mapped and described the benthic megafauna and benthopelagic fish fauna at Valdivia Bank and Ewing Seamount as part of an extended survey of different southeast Atlantic seamounts. Recent advances in other areas provided first insights of meso- and benthopelagic fish dynamics at remote seamounts in the South Atlantic from a combination of fisheries acoustic methods and pelagic trawl sampling (Campanella et al., 2021). As part of the Ecosystem Approach to Fisheries (EAF)-Nansen Program, the South East Atlantic Fisheries Organisation (SEAFO) and its partners have conducted surveys in 2015, 2019, and 2022 aiming at identifying and mapping vulnerable marine ecosystems (VMEs) and fisheries resources at the South-West Discovery Seamounts and the North Guinea Seamount chain in the South Atlantic (SEAFO, 2019, 2022). Despite these recent advances, the South Atlantic is still considered as an area poor in data on physical oceanography, benthic species, and benthic ecosystem functioning (Bridges, Howell, et al., 2023). Modern dynamic basin-scale ocean models, spatially explicit broad-scale benthic habitat classification techniques, and multivariate benthic landscape maps extending from coastal areas to areas beyond national jurisdiction (ABNJ) have been increasingly used to narrow existing data and knowledge gaps in the southeast Atlantic (McQuaid et al., 2023; Rühs et al., 2019; Schumacher et al., 2022; Tim et al., 2018).

The capacity to predict benthic species distributions requires knowledge of functional relationships between ecosystem components, terrain attributes, and changes in physical and biogeochemical water properties over space and time but may also consider the role of physical processes and mechanisms that drive food supply (Mohn et al., 2023; Pearman et al., 2023). Seamounts interact with the surrounding flow field, generating a wide range of physical processes across various frequencies. These processes include intensified turbulent mixing, internal wave dynamics, and seamount-trapped waves (Haidvogel et al., 1993; Kunze & Toole, 1997; Vlasenko et al., 2018). The transfer and conversion of kinetic energy from lower to higher frequency motions is strongly enhanced over complex and abrupt topography in the ocean interior including seamounts (Lavelle & Mohn, 2010; Nikurashin et al., 2013; Thorpe, 2007). This dissipation of kinetic energy from barotropic tides to turbulence promotes mixing of food items through the water column and enhances particle encounter rates of feeding corals and sponges (Maier et al., 2023; van der Kaaden et al., 2021).

In this study, we integrate physical data from high-resolution nested implementations of the hydrodynamic ROMS-AGRIF model (Shchepetkin & McWilliams, 2005) with observed occurrences of Cnidaria (passive suspension feeders) and Porifera (active suspension feeders) in the near-bottom layers at Valdivia Bank and Ewing Seamount. These two phyla are key structuring organisms in deep-sea benthic ecosystems (Maldonado et al., 2017; Orejas et al., 2017; Roberts et al., 2006), as they form three-dimensional habitats for other organisms, creating marine animal forests (Orejas et al., 2022; Rossi et al., 2017). We hypothesize that physical mechanisms driving food supply play a key role in determining the spatial distribution of benthic suspension-feeding communities. Although we are not examining differences between active and passive feeding strategies, we select these phyla to broaden the scope of our hypotheses across a diverse range of suspension-feeding organisms. We describe the dominant oceanographic patterns and their spatial and temporal variability in each area and investigate the potential biophysical connections and physical drivers of cnidarian and sponge distribution at Valdivia Bank based on daily averaged and 3-hourly instantaneous current velocity data.

The local embedded hydrodynamic models have a resolution of 1,500 m (parent grid) and 500 m (child grid) and receive input from high-resolution bathymetry, barotropic tides, and water mass properties. The region is connected to the open ocean, in particular the South Atlantic subtropical gyre and the influence from the Indian Ocean through the Agulhas Current system, called Agulhas Leakage (Rühs et al., 2022). Lateral boundary conditions of current velocities and hydrography from the basin-scale circulation are provided by output from the ocean general circulation model INALT20 at a resolution of 1/20° (Rühs et al., 2022; Schwarzkopf et al., 2019). Large eddies

may interact with seamounts and other abrupt topographic features at various levels during collision or near-collision events. Such interaction may include trapping of eddies followed by changes in the local dynamics and spawning of smaller eddies as observed for Meddies in the North Atlantic (Bashmachnikov et al., 2009; Shapiro et al., 1995) as well as eddy splitting and destruction (as reported for Agulhas Rings at Vema Seamount in the southeast Atlantic; Schouten et al., 2000). Encounters between eddies and seamounts can episodically influence seamount faunal communities by increasing or decreasing food availability through upstream entrainment and advective loss (e.g., Drazen et al., 2011).

2. Materials and Methods

2.1. Study Sites

Valdivia Bank takes the shape of an elongated oceanic plateau and is located at the northeast Walvis Ridge, a large ridge system in the SE Atlantic intersected by canyons and seamounts separating the Angola Basin to the North from the Cape Basin to the South (Figure 1a). The Valdivia Bank plateau has an elliptical shape with water depths from 220 m to more than 4,000 m in the surrounding abyssal plains (Bergstad, Høines, et al., 2019; Contreras et al., 2022). The entire plateau extends over a length of 360 km in the N-S direction (major axis) and 220 km in the E-W direction (minor axis). The bank morphology is characterized by generally gentle slopes of <1°, but there are several areas where slopes are significantly steeper exceeding 30°. Along these steep slopes abrupt increases in depth of 1,500 m or greater are common (Contreras et al., 2022). The central summit plateau is composed of smaller areas with distinct topographic elevations of different sizes and heights. A prominent seamount-like feature is located at the southern plateau at approximately 6.4°E and 26.2°S (Figure 1b, sampling area D). This seamount is elongated in the NE-SW direction and has the form of a flat-topped guyot bounded by steep slopes with water depths in the range 220–1,000 m. In contrast, Ewing Seamount is an isolated seamount located off the northeastern part of the Walvis Ridge in the northern Cape Basin centered at 23.245°S and 8.27°E (Figure 1c). It has a diameter of approximately 30 km with an irregular bottom relief shaped by inlets and rifts along the deeper slopes. The summit plateau covers the depth range 850–1,000 m with the smallest peak at 780 m water depth.

2.2. Hydrodynamic Models

The Regional Ocean Modeling System with grid refinement (ROMS-AGRIF, here the version 3.1) was used to simulate currents and water mass properties at Valdivia Bank and Ewing Seamount with high resolution increasing across two levels of nested grids of 1,500 and 500 m in each study area (Figures 1b and 1c). ROMS-AGRIF is a free surface, finite difference, primitive equation model applying orthogonal curvilinear coordinates on a staggered Arakawa C-grid in the horizontal and stretched sigma coordinates (s-coordinates) in the vertical (Shchepetkin & McWilliams, 2005). The ROMS-AGRIF model receives initial conditions and lateral boundary conditions from the global nested model INALT20 (Schwarzkopf et al., 2019). Lateral boundary conditions are prescribed as 5-day averages of current velocities, sea surface height, temperature, and salinity. INALT20 is a global eddy-permitting (1/4°) ocean/sea ice model configuration based on NEMO (Nucleus for European Modeling of the Ocean) with a high-resolution eddy-rich nest (1/20°, 46 vertical z-levels varying between <10 m close to the surface and 250 m at water depths >5,000 m) covering the South Atlantic and the western Indian oceans between 70° W and 70° E and extends from the northern tip of the Antarctic Peninsula at 63° S to 10° N (Schwarzkopf et al., 2019). For our local simulations, we used a hindcast simulation (referred to as SIM_{JRAO} in Rühs et al., 2022) driven by the recent atmospheric forcing product JRA55-do (Tsujino et al., 2018) following the OMIP2 protocol (Tsujino et al., 2020). The OSU (Oregon State University) inverse tidal model provides instantaneous sea surface height and barotropic velocities for 10 tidal constituents (Egbert & Erofeeva, 2002) through radiation terms along the open lateral boundaries. Local solutions of water mass properties and currents from the parent grids at 1,500 m resolution are transferred to the child grids at 500 m resolution at every time step. Explicit lateral viscosity is zero everywhere in the models except one grid cell wide sponge layer on each grid to reduce numerical instabilities along the open boundaries. COADS (Comprehensive Ocean-Atmosphere Data Set, 0.5° × 0.5° spatial resolution) data was used as background atmospheric forcing at the free surface to supplement the lateral boundary conditions from INALT20. The total simulation time was set to four years covering the period 2007 to 2010. The largest model time step is 90 s, which is sufficient to capture tidal dynamics as a potentially important physical driver at these sites. The bathymetry used in the model is an integrated data set from multi-beam surveys collected between 2008 and 2010 by IEO-CSIC as part of the RAP-SUR project in both study areas and merged with depth information from the GEBCO_2020 global bathymetry at a spatial resolution of 15
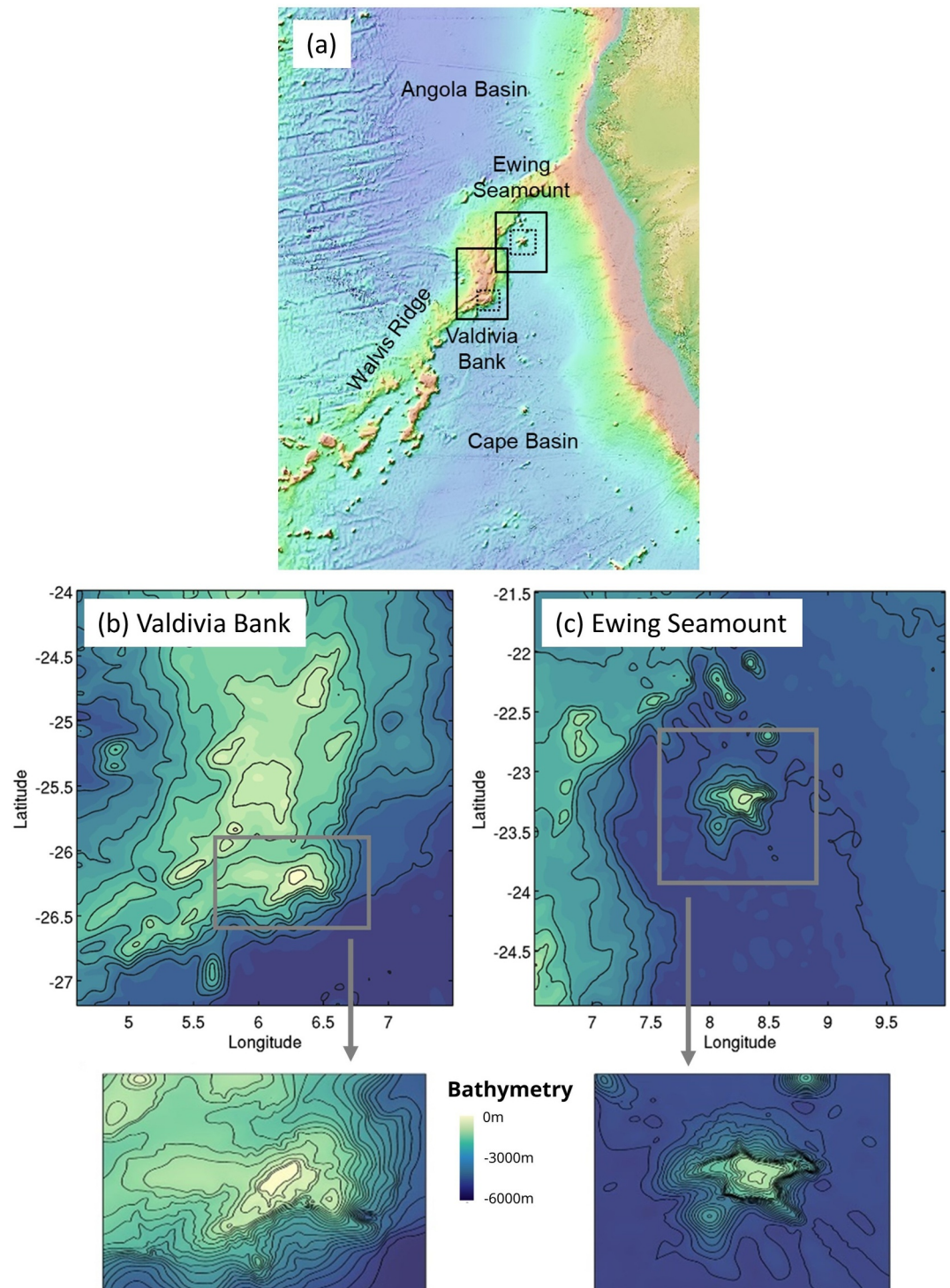
Figure 1. (a) Location of the two study sites along the Walvis Ridge in the SE-Atlantic. The ROMS-AGRIF hydrodynamic model employs embedded grids to locally increase spatial resolution from 1,500 m (parent grid) to 500 m (child grid) with enhanced bathymetry at Valdivia Bank (b) and Ewing Seamount (c).

arc s. GEBCO_2020 was the most recent version of global bathymetry at the time of the model setup. The integrated bathymetry has a spatial resolution of 250 m. This bathymetry in combination with improved spatial resolution in the local nests allows a more detailed view of physical processes over complex topography in the

Table 1
Grid Metrics (Size of Model Area and Number of Grid Cells) of Local High-Resolution ROMS-AGRIF Model Implementations as Shown in Figures 1b and 1c

Grid metrics	Valdivia bank (parent grid)	Valdivia bank (child grid)	Ewing seamount (parent grid)	Ewing seamount (child grid)
Horizontal resolution (m)	1,500	500	1,500	500
Grid size [lon, lat] (km)	297 × 363	115 × 91	357 × 387	133 × 133
Grid points [lon, lat]	198 × 242	230 × 182	238 × 258	266 × 266
Longitude range (°E)	4.6 to 7.5	5.6 to 6.8	6.5 to 10.0	7.5 to 8.85
Latitude range (°N)	−27.19 to −23.76	−26.61 to −25.813	−24.96 to −21.488	−23.871 to −22.677

central seamount areas of Valdivia Bank and Ewing Seamount (Figures 1b and 1c). All nested model implementations have 32 terrain-following vertical layers (s-layers) with higher resolution close to the surface (stretching parameter $\theta_s = 3.4$) and bottom ($\theta_b = 1.0$). The near-bottom vertical resolution of s-layers varies between <2 m in the shallowest areas and 39.5 m in the deepest areas of Valdivia Bank. At Ewing Seamount, the corresponding difference in near-bottom vertical resolution changes from 6.5 to 38 m, respectively. The grid metrics are summarized in Tables 1 and 2, respectively.

### 2.3. Benthos, Water Mass Properties, and Cape Basin Circulation

Spatially resolved data on megabenthos (Cnidaria and Porifera) and physical oceanography were collected during several Spanish-Namibian surveys in the years 2008, 2009, and 2010 on board the B/O Vizconde de Eza. These surveys were conducted as part of the RAP-SUR project, which aimed to identify and characterize vulnerable marine ecosystems (VMEs) associated with seamounts inside the SEAFO Regulatory Area (Durán Muñoz et al., 2012; López-Abellán & Holtzhausen, 2011). The two seamounts were investigated again in 2015 as part of an extended survey of South Atlantic seamounts on the board RV Fridtjof Nansen (Bergstad, Gil, et al., 2019, Bergstad, Høines, et al., 2019). Analysis of samples from benthos surveys at Valdivia Bank and in the Ewing Seamount in the periods 2008, 2009, and 2010 (box-corer, rock-dredge, video and still photographs) showed the occurrence of a large number of taxa, many of them benthic suspension feeders (López-Abellán & Holtzhausen, 2011). In our analysis, we only considered Cnidaria and Porifera, as these groups include important VME indicator species (cold-water corals (CWCs) and sponges; Figure 2). Cnidarians were represented by several taxa, including octocorals (i.e., bamboo corals belonging to the family Isididae) and scleractinians (i.e., *Enallopsammia rostrata*). Sponges were represented mostly by hexactinellids and demosponges. Bergstad, Gil, et al. (2019) describe a large diversity in benthic megafauna associated with southeast Atlantic seamounts including ancient scleractinian coral framework and rubble. Samples collected during the RAP-SUR expeditions corroborate these observations, revealing a remarkable occurrence of cnidarians, including cold-water corals (CWCs) as well as sponges (Figure 2a). Camera surveys at Valdivia Bank showed that live corals were very patchily distributed, and numbers often decreased toward the summits except for the shallow southeast Valdivia summit, where numerous gorgonians were detected (Bergstad, Gil, et al., 2019, Figure 2a). At Ewing Seamount, scattered live corals (scleractinians, gorgonians, and antipatharians) were recorded during all camera surveys with again decreasing numbers at the seamount summit (Bergstad, Gil, et al., 2019). Large aggregations of cnidarians during the RAP-SUR surveys were reported at the western summit region (Figure 2b).

CTD data from the Valdivia Bank and Ewing Seamount were collected during the 2008, 2009, and 2010 RAP-SUR benthos surveys (station locations are shown in Figure S1 in Supporting Information S1 Section). Below, we

Table 2
Resolution (m) of the Bottom-Most Vertical s-Layers for Each Model Grid Over Different Parts of the Model Bathymetry (h_{min} = Minimum Depth in Each Model Grid, h_{max} = Maximum Depth in Each Model Grid)

| Grid	Δz (bottom) at h_{min}	Δz (bottom) over slopes	Δz (bottom) at h_{max}
Valdivia parent	1.3	20.4	39.5
Valdivia child	1.8	20.4	39.0
Ewing parent	6.5	22.4	38.2
Ewing child	6.7	22.1	37.5
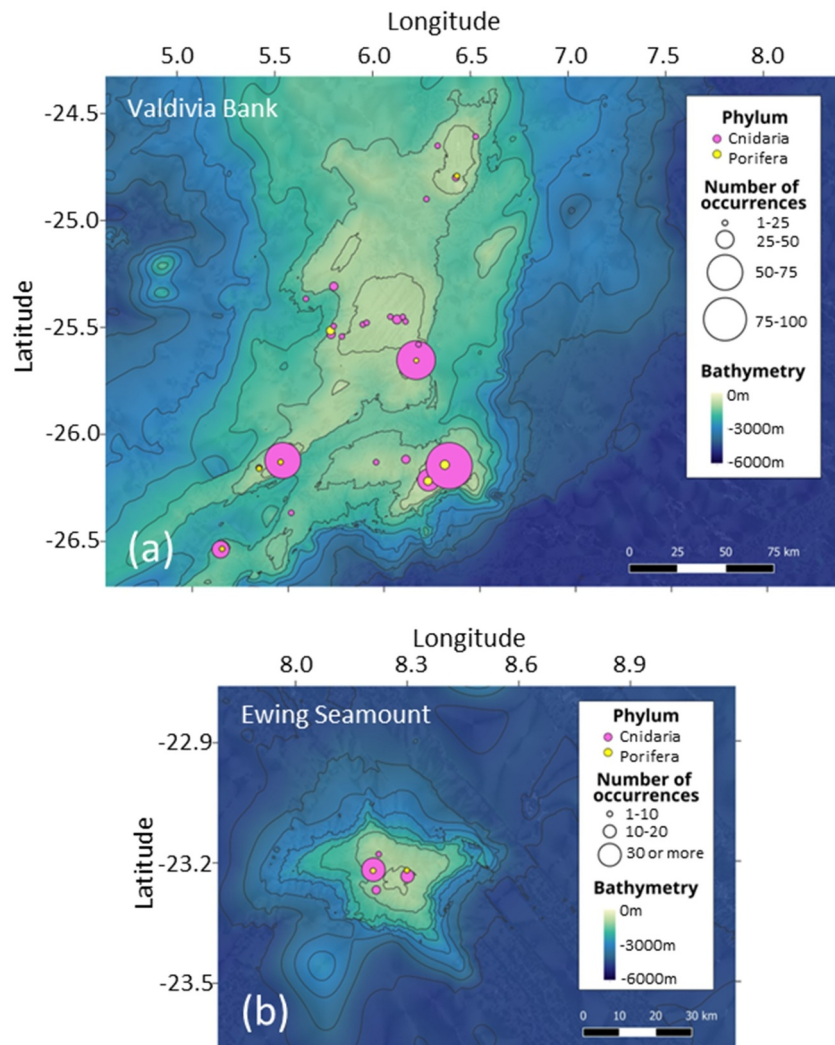
Figure 2. Cnidaria (magenta circles) and Porifera (yellow circles) occurrences at Valdivia Bank and Ewing Seamount from surveys conducted in the period 2008, 2009, and 2010 by IEO-CSIC (Spain) as part of the RAP-SUR project (López-Abellán & Holtzhausen, 2011). Black contour lines represent water depths. Cnidaria species distributions at Valdivia Bank are shown in Figure S5 in Supporting Information S1 section.

only present CTD data from Valdivia Bank that was used for model validation. The water mass characteristics in the Valdivia Bank region correspond to properties found in other areas of the South Atlantic (Figure 3b). Eastern South Atlantic Central Water (ESACW) is the main water mass in the upper layer and is centered in the depth range 200–700 m. In the Valdivia Bank region, ESACW covers the range $\theta = 6–15°C$ and $S = 34.5–35.4$, respectively, at densities $\sigma_\theta = 26.2–27.1 \text{ kg m}^{-3}$ (Figure 3b). ESACW is formed southwest of South Africa, where waters from the Indian Ocean mixes with the South Atlantic Current (SAC) inside an area from 30 to 40°S and 0–20°E (Figure 3a; Liu & Tanhua, 2021). The SAC feeds the north-westward flowing Benguela Current (BC) with relatively cold and oxygen-rich ESACW. The BC continues along the Southwest African margin before being deflected westward south of the Angola-Benguela Frontal Zone (Figure 3a; Mohrholz et al., 2014). The minimum θ and S inflection point at $\theta = 4°C$, $S = 34.4$, and $\sigma_\theta = 27.3 \text{ kg m}^{-3}$ represent the influence of Antarctic Intermediate Water (AAIW). AAIW is formed in the surface region north of the Antarctic Circumpolar Current (ACC) from where it subducts and propagates northward, whereas it is modified through mixing with surrounding water masses (Liu & Tanhua, 2021; Stramma & England, 1999). Below 1,200 m depth, the increase in salinity until the deep salinity maximum $S = 34.85$ can be attributed to North Atlantic Deep Water (NADW), which covers the depth range 1,200–2,000 m in the South Atlantic and is composed of characteristic water masses from the North
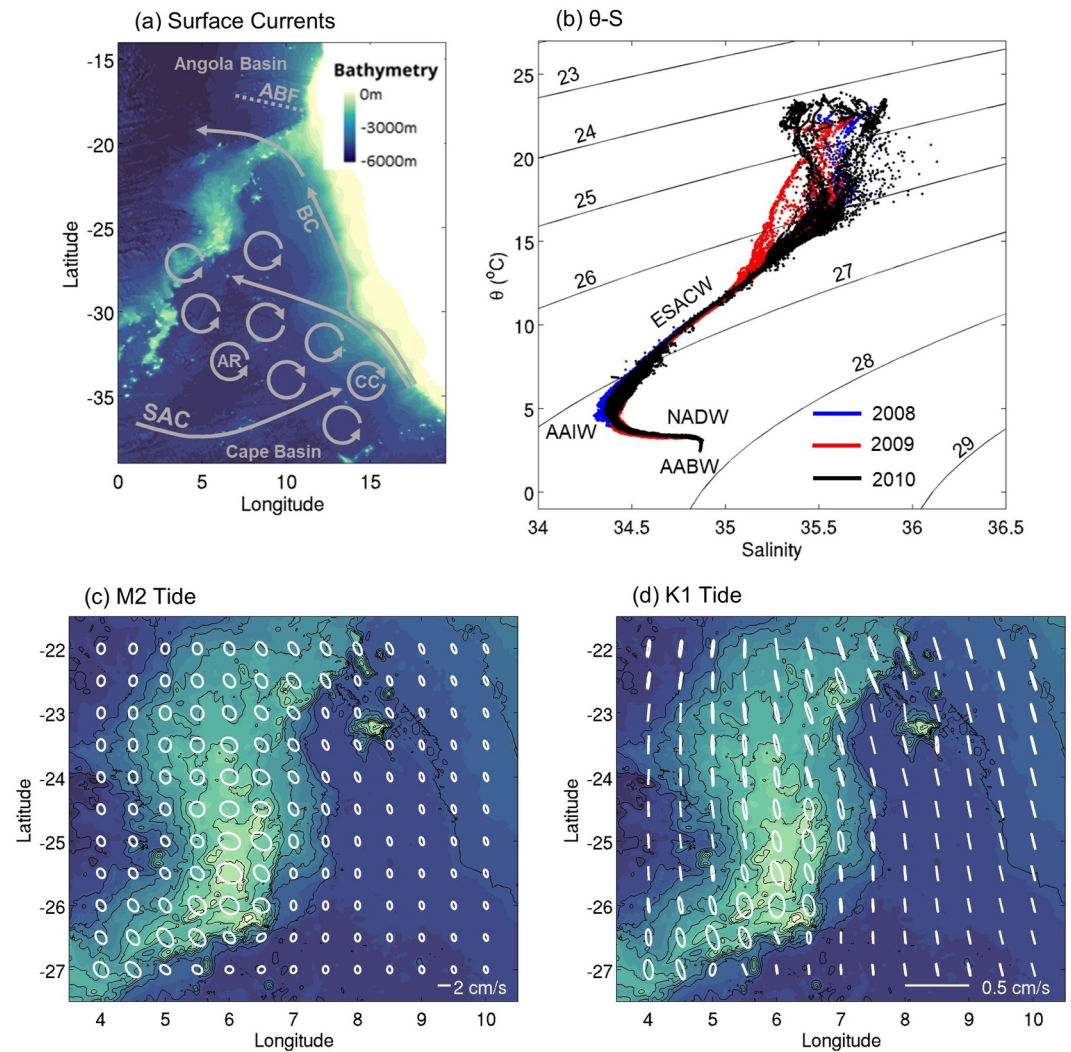
Figure 3. (a) Schematic of the main surface circulation features in the SE Atlantic (ABF = Angola-Benguela-Front, AR = Agulhas Rings, BC = Benguela Current, and CC = Cape Cyclones). (b) θ—S diagram based on Valdivia Bank CTD data from the 2008–2010 RAP-SUR surveys (López-Abellán & Holtzhausen, 2011). Colored dots indicate data from different years, and black lines denote isopycnals of density anomaly σ_θ (kg m^{-3}). The water masses are Eastern South Atlantic Central Water (ESACW), Antarctic Intermediate Water (AAIW), North Atlantic Deep Water (NADW) and Antarctic Bottom Water (AABW). Current ellipses for the barotropic tidal harmonics M2 (c) and K1 (d) tides from the Atlantic solution AO_atlas (1/12° spatial resolution) of the Oregon State University Tidal Inversion Software (OTIS). Colored contours represent bathymetry, and black lines show depth contours from 500 to 6,000 m in 500 m intervals. The CTD station locations are shown in Figure 1 in Supporting Information S1 section.

Atlantic overflow regions (Liu & Tanhua, 2021; and references therein). The deepest waters in the Valdivia Bank region showed inflections of Antarctic Bottom Water (AABW) at a temperature minimum of $\theta = 2.8°C$. AABW is formed in the Weddell Sea region through mixing of Circumpolar Deep Water (CDW) and Weddell Sea Bottom Water (WSBW) (van Heuven et al., 2011). The current system surrounding Valdivia Bank and Ewing Seamount is influenced by the anticyclonic circulation in the South Atlantic subtropical gyre (Chidichimo et al., 2023), entering from the southeast, warm, and salty waters of Indian Ocean origin entering the Atlantic Ocean through Agulhas Leakage (Rühs et al., 2022). This happens as a direct inflow but also in the form of large mesoscale eddies. These Agulhas Rings represent one of the largest mesoscale eddies in the world ocean with diameters of more than hundred kilometers and depth extensions of 1,000 m and more (Casanova-Masjoan et al., 2017). The Walvis Ridge lies to the northeast of the main route of Agulhas Rings as they drift into the South Atlantic (Dencausse et al., 2010). Although very few anticyclonic eddies entered the southwestern part of our model area during the course of the experiment, their warm and saline footprint is still visible (Figure 3b).

Table 3
Summary of Descriptors and Proxy Metrics Used to Investigate Near-Seabed Bio-Physical Connections (See Section 4.4)

Descriptor	Calculation	Description	Processes influencing food supply
Mean current velocity U_{mean}	U_{mean} (m s^{-1}), $U = \sqrt{u^2 + v^2}$	Three-year (2008–2010) average calculated from daily averaged model outputs of velocity components u and v on a 1,500 m resolution grid.	Advection and retention of lateral food input (quantity and speed).
Maximum current velocity U_{max}	U_{max} (m s^{-1}), $U = \sqrt{u^2 + v^2}$	Three-year (2008–2010) maximum at each model grid point calculated from daily averaged model outputs of velocity components u and v on a 1,500 m resolution grid.	Advection and retention of lateral food input (quantity and speed) during episodic peak events (feast-famine conditions).
Kinetic energy dissipation rate ε	$\varepsilon = \rho \cdot A_h\left[\left(\frac{\partial U}{\partial x}\right)\cdot\left(\frac{\partial U}{\partial x}\right) + \left(\frac{\partial U}{\partial y}\right)\cdot\left(\frac{\partial U}{\partial y}\right)\right] + \rho \cdot A_v\left[\left(\frac{\partial U}{\partial z}\right)\cdot\left(\frac{\partial U}{\partial z}\right)\right]$	Three-year (2008–2010) average calculated from daily averaged model output of the modeled 3D velocity (u,v, w) field based on Nikurashin et al. (2013). The horizontal viscosity $A_h = 1$ m^2 s^{-1} and vertical viscosity $A_v = 10^{-3}$ m^2 s^{-1} are background values accounting for the aspect ratio in momentum exchange (Nikurashin et al., 2013). The density of seawater ρ (kg m^{-3}) is calculated from the modeled temperature and salinity fields.	Vertical mixing and particle encounter rates. Time how long food particles stay in suspension and available.
Internal wave slope criticality S	S = h/c	$c = \sqrt{\frac{\omega^2 - f^2}{N^2 - \omega^2}}$, with M2 tidal frequency $\omega = 1.4053e{-}4$ s^{-1} and inertial frequency f (Cacchione et al., 2002; St. Laurent & Garrett, 2002). The Brunt-Väisälä frequency N was calculated from daily averaged model output of temperature and salinity. The topographic slope h is derived from the 1,500 m model grid topography, averaging gradients in longitude and latitude over each grid cell.	Direction and intensity of internal wave propagation (reflection, transmission, local amplification). Enhanced vertical mixing and food particles in suspension through breaking internal waves and turbulence in near-critical conditions ($S \approx 1$).

The characteristics of dominant barotropic semidiurnal (M2, period = 12.4 hr) and diurnal (K1, period = 23.9 hr) tidal harmonics across the Valdivia Bank area are shown in Figures 3c and 3d. The ellipses of the principal M2 tide are largely directed along-slope (NNW to SSE) in the deep basins but are amplified and less rectified over the shallower Valdivia Bank. The magnitude of the M2 major axis is larger by one order of magnitude than the K1 major axis. The magnitude of the dominant semidiurnal tidal harmonic M2 is up to 2 cm s^{-1} above the shallower areas of the Valdivia Bank between 5°E and 7°E and −23°S and −27°S, whereas corresponding values in the Cape Basin do not exceed 1.1 cm s^{-1} (Figure 3c). The main diurnal tidal harmonic K1 is an order of magnitude smaller (maximum semimajor axis 0.2 cm s^{-1}) and is strongly rectified in a North-South direction (Figure 3d).

2.4. Metrics of Physical Descriptors of Food Supply for Benthic Suspension Feeders

The conversion and dissipation of kinetic energy of currents at complex topographic structures generates energetic internal tide dynamics and vertical mixing, which may help to establish a steady food supply for cnidarians and sponges by sustaining a high encounter rate with food particles. The relative steepness of the topographic slope to the angle of internal tidal wave propagation is a key factor influencing the generation and modification of internal tides at the site (Cacchione et al., 2002; St. Laurent & Garrett, 2002). The topographic slope (h) is considered critical or near-critical when its steepness matches or is close to the steepness of the internal wave beam angle (c). At critical slopes, the internal tide resonates, and vertical mixing is intensified. At gentler subcritical slopes (h < c), internal waves pass the topographic slope without significant interference. At steeper supercritical slopes (h > c), internal waves are reflected and may advect food particles over larger distances (see Table 3 for the computation of internal wave slope criticality). Kinetic energy dissipation rates and internal tide characteristics at the spatial scales of the model are estimated from daily averages of the modeled 3D temperature, salinity, and velocity field as described in Table 3. In addition, we compared kinetic energy dissipation rates from

daily averaged velocities with dissipation rates from 3-hourly instantaneous velocities to estimate the importance of temporal resolution in resolving tidal effects.

3. Results

3.1. Model-Data Comparison

Water mass properties from CTD data measured from 2008, 2009, and 2010 in different subregions of Valdivia Bank were compared with corresponding model data (see Figure S1 in Supporting Information S1 section for an overview of CTD station locations and sampling years). Daily averaged potential temperature and salinity profiles at grid cells nearest to the CTD station locations from both the local area ROMS-AGRIF model (parent grid, 1,500 m spatial resolution) and the global nested model INALT20 (1/20° spatial resolution, corresponds to a length scale of approximately 4 km) were used for this comparison. A statistical model skill assessment (Supporting Information S1 section) showed generally very good to good agreement between daily averaged model data and the measured short-term snapshots of temperature and salinity properties in 2009 (Figure 4) and all other sampling years at water depths >150 m and the temperature and salinity range $\theta < 17°C$, $S < 35.5$ (see Table 1, Text and Figures S1 and S2 in Supporting Information S1 section of this article). There are some notable differences between modeled and observed water mass properties in near-surface waters. In 2008 in area C, for example, both models failed to accurately reproduce the observed thermocline and halocline in the upper 150 m of the water column as well as the occasionally very high salinities of up to 36 (Figure S1 in Supporting Information S1 section). Additional differences between modeled and observed water mass properties can be attributed to the space-time bias between the CTD point measurements and model data representing conditions inside an entire grid cell as well as the intrinsic variability in the CTD data from near-surface processes and partial tidal signals that are not resolved by the time-averaged model data. In summary, we generally found good agreement between modeled and observed water mass properties that represent a longer term and quasi-steady state in contrast to short-term variability that can be attributed to short-term changes in near-surface processes and only partially resolved tidal signals.

3.2. The Large-Scale Eddy Field

The SE Atlantic south of the Walvis Ridge is a major pathway for warm waters rich in salinity, which originate in the Indian Ocean and propagate into the South Atlantic through leakage of the Agulhas Retroflection as a combination of large anticyclonic eddies (Agulhas Rings), cyclonic eddies, and direct inflow (Rühs et al., 2022). To estimate possible eddy seamount encounters at Valdivia Bank and Ewing Seamount, we analyzed sea surface height data from AVISO altimetry and the INALT20 simulations, which were used as boundary conditions for the local area ROMS-AGRIF seamount models. Figure 5 shows eddy statistics for both data sets, provided as eddy presence times (in days) in the wider study area using an eddy detection algorithm (Chelton et al., 2011). Typical eddy structures within our region of interest can be described by their sizes being smaller than 300 km and amplitudes above 5 cm. These thresholds were used to label eddies (Rühs et al., 2022), although spurious dis and reappearance of eddies might occur in cases where for example, their amplitude intermittently falls below the respective threshold. All detected eddies, regardless of size and amplitude over the years 2007–2010, were considered for anticyclonic and cyclonic rotation separately. The corresponding eddy statistics for individual years can be found in Figure S3 and S4 in Supporting Information S1 section. The results show that anticyclonic eddies propagate from their spawning area in the Agulhas Retroflection north-westward into the southeast Atlantic inside a well-defined corridor, which rarely extends northward to Valdivia Bank and Ewing Seamount. This spreading pattern is clearly visible in both data sets (Figure 5a). Encounters of anticyclonic eddies with the Valdivia Bank were limited to rather short-lived occasions in individual years (residence times 31 and 5 days for INALT20 and AVISO, respectively, in 2007; 7 and 10 days in 2009; Figure S4 in Supporting Information S1 section). There was no evidence of anticyclonic eddies close or at Ewing Seamount in any of the data sets in the period 2007–2010 (Figure 5a). The main pathway of cyclonic eddy propagation is northward entering the Benguela Current system after spawning from the Agulhas Retroflection (Figure 5b). Events of cyclonic eddy encounters with Walvis Ridge seamount topography are again very short-lived and could only be detected in AVISO data (25 days in 2008, 5 days in 2009 and 55 days in 2010; Figure S5 in Supporting Information S1 section).
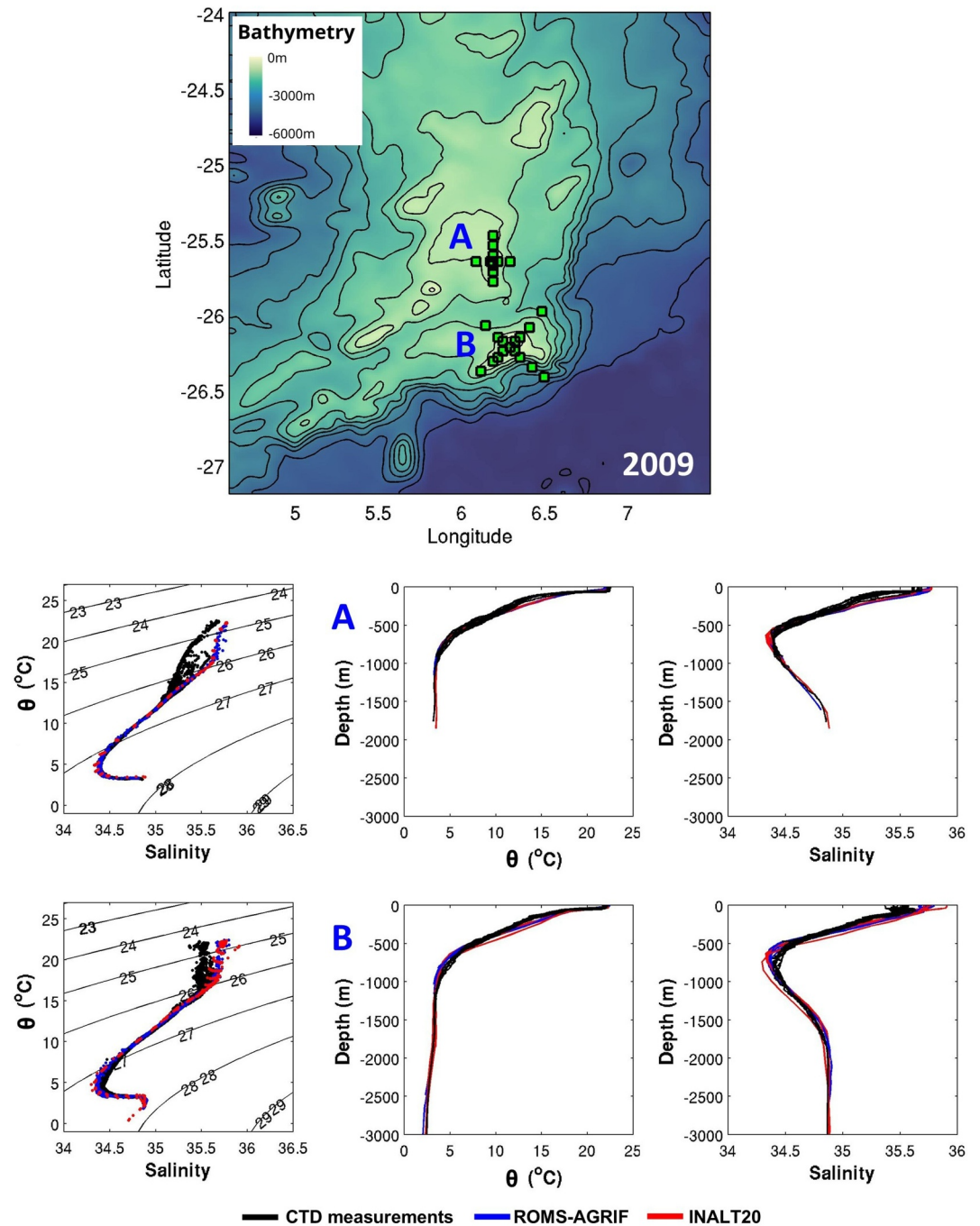
Figure 4. Observed and modeled water mass properties potential temperature θ (°C) and salinity based on CTD measurements obtained in 2009 in two sub-regions of Valdivia Bank. The subplots show θ-S diagrams and depth profiles of potential temperature θ and salinity, respectively. Corresponding model-data comparisons for the years 2008 and 2009 are presented in Supporting Information S1 section.

3.3. Near-Bottom Currents

The time-averaged near-bottom currents, simulated at a resolution of 1,500 m in the extended Valdivia Bank region, show a complex pattern influenced by variations in the underwater landscape. The near-bottom flow is shaped by shallow elevations, enclosed basins, and steep slopes plunging into the deep sea (Figure 6a). The strongest bottom currents in the model occur along the steep eastern slopes of the Valdivia Bank complex,
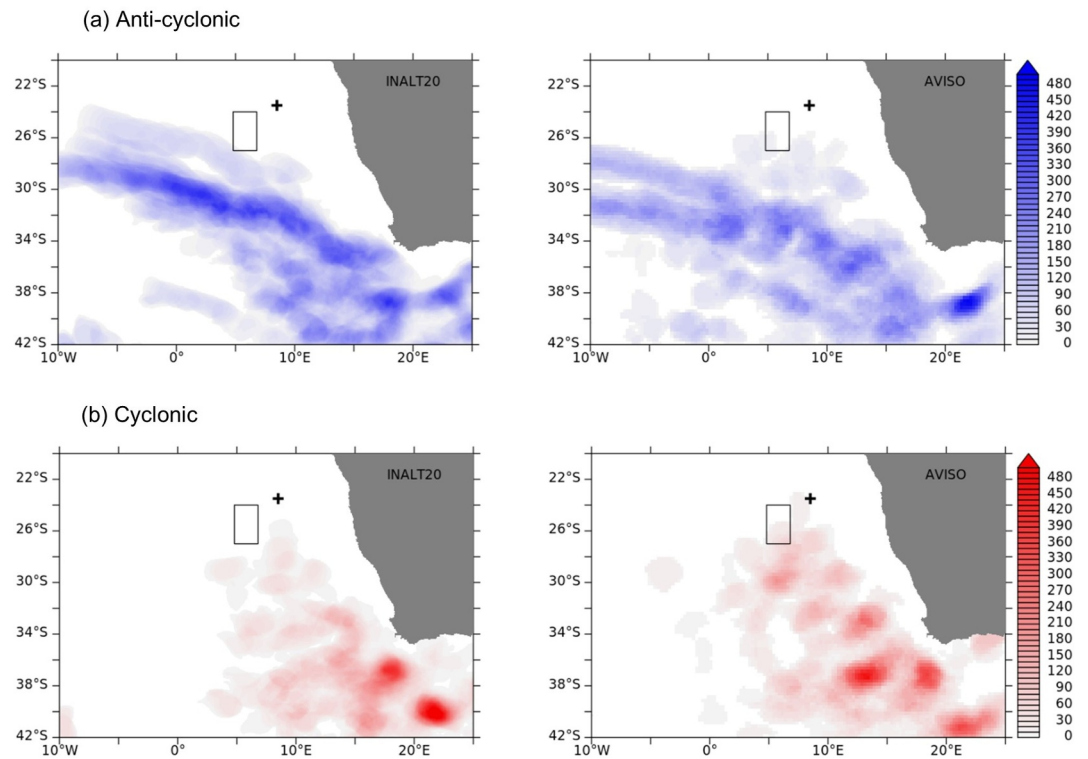
Figure 5. (a) Propagation of Agulhas Rings (anticyclonic) and (b) cyclonic eddies from the Agulhas Retroflection into the Cape Basin from 2007 to 2010 based on INALT20 model and AVISO altimetry data analysis using an eddy detection algorithm. The color scale represents residence times in days. The black rectangle indicates the location of Valdivia Bank, and the black plus sign indicates the location of Ewing Seamount.

forming part of a northward-flowing current with average speeds of 0.1–0.12 m s^{-1}. Additionally, strong currents are predicted within a narrow passage in the southwestern region of the Valdivia Bank with mean current speeds of 0.25 m s^{-1} (Figure 6a). The near-bottom circulation at the bank is largely constrained by the size and shape of the shallower topographic structures. The most prominent circulation feature is attached to topography on the Valdivia Bank and takes the shape of a time-mean anticyclonic (counter-clockwise) and largely symmetric recirculation along the slopes of the largest summit atop Valdivia Bank with current speeds of 0.06–0.08 m s^{-1} (see currents inside the gray rectangle in Figure 6a).

In the extended Ewing Seamount area, the model results again show a focusing of near-bottom currents along steeper topographic gradients. The near-bottom circulation is dominated by a northeastward flow along the Walvis Ridge in the northwestern Cape Basin with maximum 3-year mean velocities of 0.06 m s^{-1} and a southwestward return flow above the Walvis Ridge of magnitude 0.05–0.07 m s^{-1} (Figure 6b). The strongest mean near-bottom currents in the deep northern Cape Basin (eastern boundary of the model area) also show a predominantly northward flow with an occasionally meandering structure at magnitudes of 0.01–0.03 m s^{-1}. Currents at Ewing Seamount (inside the gray rectangle in Figure 6b) are largely anticyclonic and aligned with the deeper slopes, featuring cross-isobath flow components above the seamount summit. The maximum time-mean currents at Ewing Seamount are of magnitude 0.05 m s^{-1}.

A more detailed view of near-bottom currents and variability at Valdivia Bank and Ewing Seamount is presented in Figures 7 and 8 based on results from the ROMS-AGRIF child grid simulations at 500 m spatial resolution and with improved high-resolution bathymetry. At the Valdivia Bank central summit, time-averaged bottom currents highlight again the counter-clockwise recirculation along the summit slopes in combination with pronounced cross-slope currents above the summit. The strongest along-slope mean current speeds were 0.06 m s^{-1}, whereas cross-slope flows atop the summit are intensified up to 0.1 m s^{-1} (Figure 7a). Rose diagrams of near-bottom currents at selected locations along the summit slopes confirm the presence of a stable and rectified along-slope anticyclonic flow with little variability in direction and only occasional periods of weakening and larger
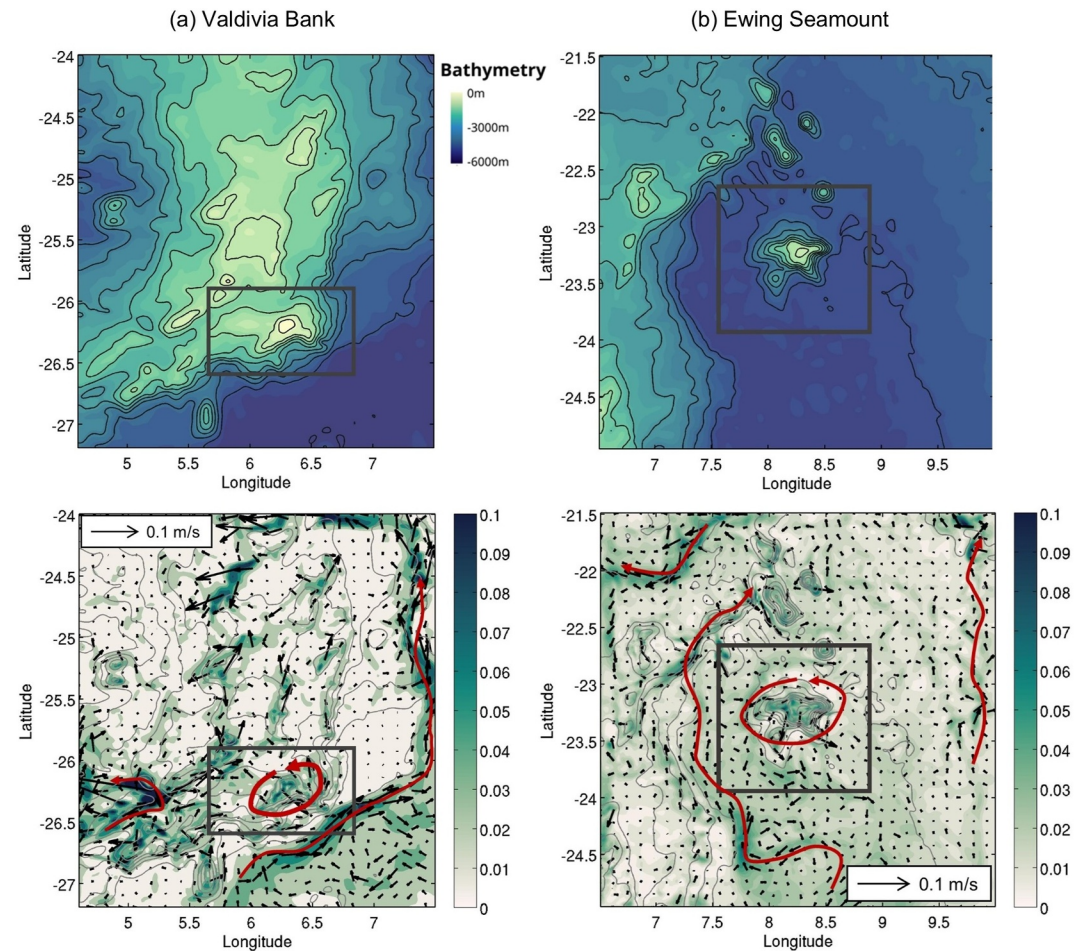
Figure 6. Model topography and composites of the time-mean near-bottom circulation in the larger (a) Valdivia Bank and (b) Ewing Seamount region simulated in the period 2008 to 2010 with the ROMS-AGRIF parent grid setup (1,500 m resolution). Shading in the top and bottom figures indicate water depth in m and current speed in m s^{-1}, respectively. Black contour lines in the top figures represent isobaths from 500 to 5,000 m at 500 m intervals. In the bottom figures, every 8th current vector is shown for improved clarity. Dark gray rectangles indicate the location of the child grid. Dark red arrows highlight the major circulation features.

changes in flow direction or flow reversal during the entire simulation period. In contrast, the model predicts tidally dominated across-slope variations with corresponding periodic changes of flow direction atop the summit (Figure 7b).

At Ewing Seamount the model predicts a mean circulation pattern similar to conditions at central Valdivia Bank with largely along-slope flow along the upper seamount slopes (1,100–1,300 m) and cross-slope flow atop the summit (Figure 8a). However, flow rectification along the slopes is less pronounced than at Valdivia Bank. Rose diagrams of Ewing Seamount currents show that currents in this depth range (with currents at 1,250 and 1,280 m depth shown as an example in Figure 8b) are still aligned with the seamount slopes in a counterclockwise sense but reveal longer periods of variability in magnitude and direction when compared to currents at central Valdivia Bank. Current velocities along the upper flanks show a typical range of 0.02–0.05 m s^{-1}. In contrast to central Valdivia Bank, modeled currents atop the Ewing Seamount summit are frequently rectified and aligned in a southwestward direction with maximum velocities in the range 0.06–0.1 m s^{-1} (Figure 8b).

### 3.4. Benthic Dynamics and Biophysical Connections at Valdivia Bank

The role of currents and their variability for supplying and replenishing benthic suspension feeder communities with organic matter and other food sources have been highlighted in many studies (e.g., de Froe et al., 2022;
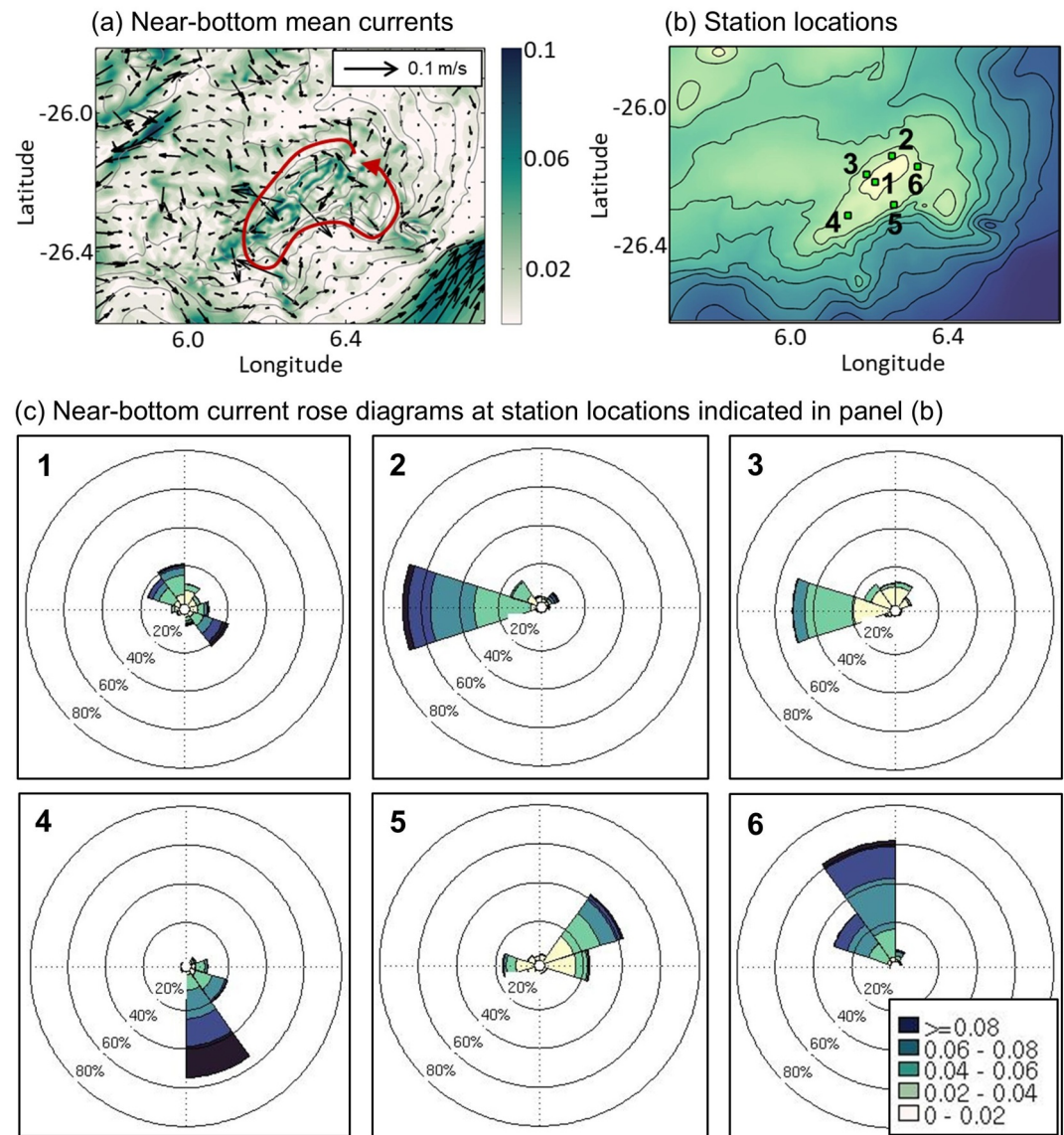
Figure 7. Near-bottom circulation at the central Valdivia Bank summit in the period 2008 to 2010 from simulations with the ROMS-AGRIF Valdivia child grid (500 m resolution). (a) Time-mean current magnitude and direction (m s^{-1}), (b) model topography and station locations for near-bottom rose diagrams calculated from daily averaged modeled current velocities (c). In (a) every 10th velocity vector is shown for clarity. The color map in (c) represents current speed in m s^{-1}.

Khripounoff et al., 2014; Mienis et al., 2007). Food supply is thought to be directly related to hydrodynamics, for example, through advection and redistribution of local-scale and far-field currents, internal tide intensified bottom currents, and turbulent mixing, bringing food particles in direct contact with the benthic organisms. In this analysis, we aim at investigating potential physical drivers of Cnidaria and Porifera distribution patterns in the Valdivia Bank area. We compare modeled water mass properties, currents, and physical mechanisms related to flow dynamics with observed occurrence (presence and randomly selected pseudo-absence) of cnidarians and sponges. Here, we will provide a basic diagnostic how well distributions of modeled near-bottom currents and different mechanistic descriptors of food supply (kinetic energy dissipation and internal wave characteristics) match the distribution of cnidarian and sponge dominated communities at Valdivia Bank. We use observed occurrences of these two groups as both form remarkable vulnerable marine ecosystems (VMEs) (FAO, 2009), and many species included in those Phyla are VME indicator species. This is for instance the case of reef forming and ecosystem engineers (sensu Jones et al., 1994) scleractinian corals (i.e., *Lophelia pertusa* aka *Desmophyllum*
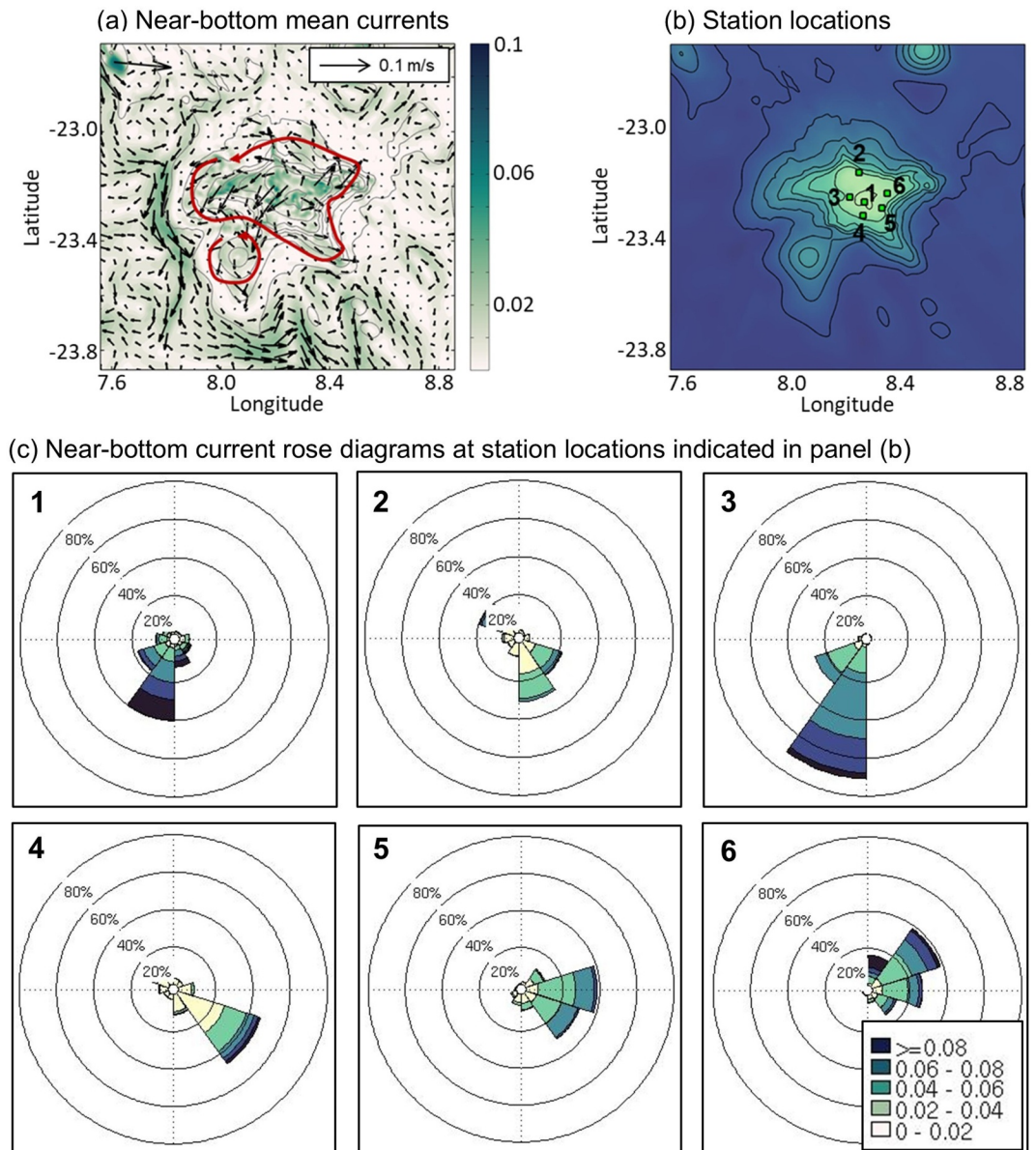
Figure 8. Near-bottom circulation at Ewing Seamount in the period 2008 to 2010 from simulations with the ROMS-AGRIF Valdivia child grid (500 m resolution). (a) Time-mean current magnitude and direction (m s^{-1}), (b) model topography and station locations for near-bottom rose diagrams calculated from daily averaged modeled current velocities (c). In (a) every 10th velocity vector is shown for clarity. The color map in (c) represents current speed in m s^{-1}.

pertusum and *Enallopsammia rostrata*). Species occurrence data were collected during the 2008, 2009, and 2010 RAP-SUR surveys (López-Abellán & Holtzhausen, 2011).

Figure 9 shows the distribution of different descriptors superimposed on observed distributions of Cnidaria and Porifera at Valdivia Bank (see Table 3). Maximum near-bottom current speeds represent the maximum value at each grid point of the model's parent grid (1,500 m resolution) over the entire simulation period (2008–2010) based on daily averaged model output. Other descriptors are calculated based on 3-year averaged model data. Larger assemblages of Cnidaria and Porifera do not seem to show preference for a specific dynamic regime defined by a characteristic range of flow magnitudes (Figures 9a and 9b). Although observed Cnidaria and Porifera occurrences exist over a limited range of modeled mean current speeds of 0.02–0.07 m s^{-1}, they are spread across a wide range of maximum current speeds (0.1–0.3 m s^{-1}).
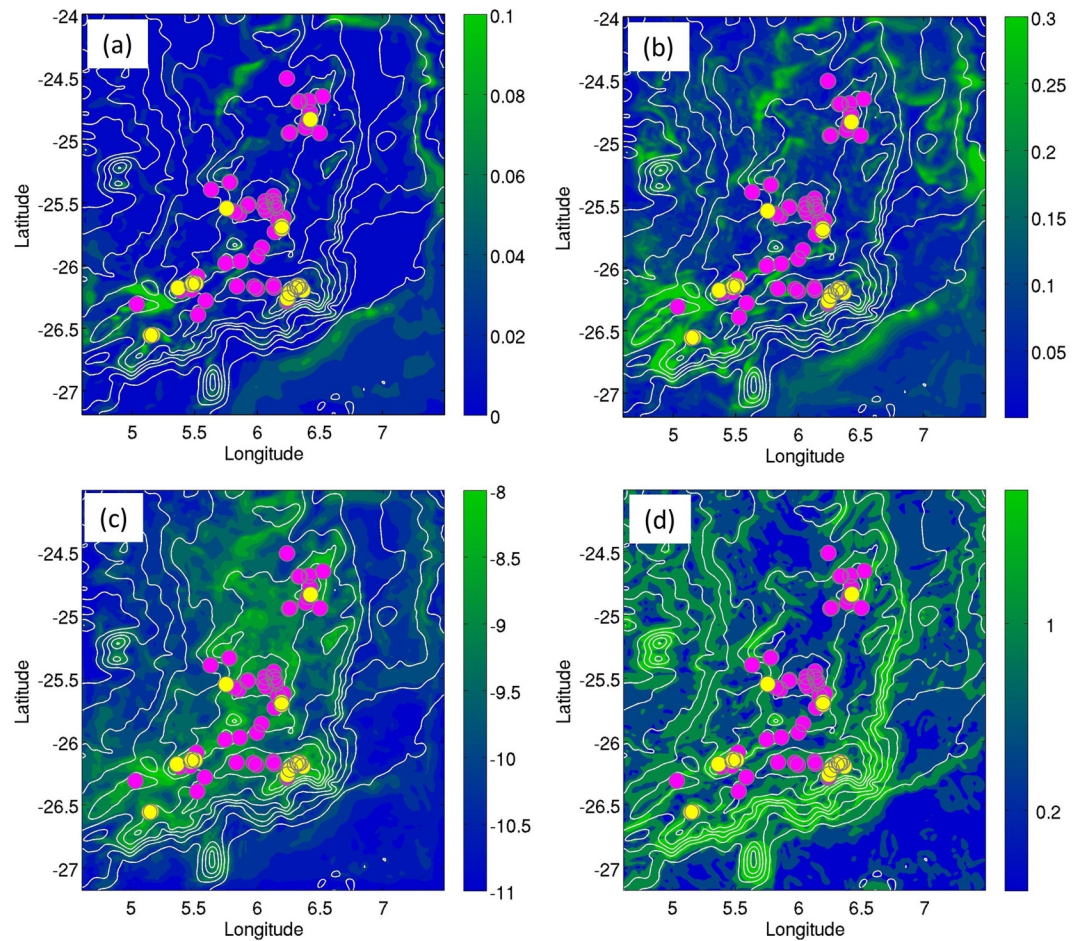
Figure 9. (a) Mean and (b) maximum current speeds (m s^{-1}), (c) mean near-bottom kinetic energy dissipation rate $\log_{10}(\varepsilon)$ (W kg^{-1}), and (d) mean values of internal wave slope criticality S superimposed on observed distributions of Cnidaria (magenta squares) and Porifera (yellow squares). All parameters were calculated from daily averaged model output of the 2008–2010 Valdivia Bank parent grid simulations. Contour lines represent depth contours at 500 m intervals in the range 500–6,000 m.

Near-bottom distributions of kinetic energy dissipation rates ε in the period 2008–2010 are presented in Figure 9c. Kinetic energy dissipation rates are enhanced above most parts of the Valdivia Bank, contrasting with low levels of ε in surrounding deep waters. Particularly, local maxima in ε can be found above the central bank summit to the southeast and in the southwestern corner of the bank. Our model findings suggest that locations of enhanced kinetic energy dissipation rates are closely connected with observed distributions of Cnidaria and Porifera occurrences: Larger aggregations of Cnidaria and Porifera are associated with areas exhibiting intensified energy dissipation rates, rarely occurring in regions where $\log_{10} \varepsilon$ values fall below −9 W kg^{-1}.

The distribution of the internal wave slope criticality S is shown in Figure 9d. Topographic slopes are critical or near-critical relative to the internal wave slope steepness c ($S \sim 1$) in areas with the highest bottom velocities. These areas encompass the southwestern part of the Valdivia Bank and the steep slopes along its margins connecting the bank to the deeper surrounding waters. Across the bulk of the Valdivia Bank complex, topographic slopes are near-critical or super-critical ($S > 1$). Areas with gentle topographic slopes ($S < 1$) mainly exist throughout the northern Valdivia Bank complex and are subcritical (transmissive) with respect to the interaction with internal waves. Our analysis shows no clear preference for specific internal tide regimes in Cnidaria distributions. In contrast, Porifera assemblages are predominantly associated with near-critical slopes (Figure 9d). However, it is important to keep in mind that the data set is limited and that the absence of species occurrences in supercritical areas is likely due to under-sampling.

A more detailed analysis of modeled environmental conditions and terrain attributes at observed taxa occurrences is presented by comparing observed occurrences (presence data) with model data selected from randomly accessed pseudo-absence locations. Pseudo-absences (sometimes also defined as environmental background data) are not considered as true absences (which were not available from the RAP-SUR sampling) but rather represent data locations outside the observed taxa presence data (Barbet-Massin et al., 2012). Presence locations for all modeled environmental variables and terrain data were approximated by calculating the positions of the model grid points, which are located closest to the locations of the observed cnidarian and sponge data. In total, 391 (Cnidaria) and 32 (Porifera) observed presence locations were identified at Valdivia Bank. In a second step, pseudo-absence locations were calculated from model data in areas outside presence locations using an equal number of randomly selected positions for each phylum. The resulting investigation describes the ranges of environmental conditions where communities of Cnidaria (Figure 10a) and Porifera (Figure 10b) occur. Cnidaria and Porifera assemblages occur in waters with a median temperature $\theta = 4$–$5°C$ and a median salinity $S = 34.5$–34.6. Conditions at random pseudo absence locations were generally lower in temperature but higher in salinity. It is important to acknowledge the potential impact of a remaining depth bias between presence and random pseudo-absence locations, despite the analysis being confined to the depth range of the recorded presence locations for both phyla (200–1,500 m). Occurrences of both phyla can be found in waters with stronger mean and maximum currents than predicted for random absence locations. The median and maximum current velocities at presence locations is 0.04–0.05 and 0.15–0.18 m s^{-1}, respectively. In contrast, median and maximum currents at pseudo-absence locations do not exceed 0.03 and 0.11 m s^{-1}. However, the distribution of Cnidaria and Porifera across the Valdivia Bank is mostly linked to internal wave slope criticalities with a median at $S \approx 1$ indicating critical or near-critical slopes with a large spreading of values in both presence and pseudo-absence data. There is a distinct difference in kinetic energy dissipation rates ε between presence and random absence locations for both phyla. ε values at presence locations are one to two orders of magnitude larger than dissipation rates at random absence locations. The combination of increased kinetic energy dissipation rates and near-critical reflection of internal waves creates a highly dynamic environment with a strong potential to redistribute organic material and increase the availability of food sources for local fauna. These dynamic conditions, where Cnidaria and Porifera are typically found, seem to be generally restricted to shallower depths and areas with steeper topographic slopes (Figure 10). Our analysis suggests that these areas are the preferred environment for cnidarian and sponge assemblages in the Valdivia Bank region. This approach may be useful in guiding future species distribution modeling aiming to refine the accuracy of model predictions. In summary, combining more traditional water properties such as temperature, salinity, and current speed with physical processes such as kinetic energy dissipation rate may help to provide a more conclusive picture of biophysical connections for benthic suspension feeders communities: larger aggregations of Cnidaria and Porifera occurrences appear to be mainly connected with areas of intensified kinetic energy dissipation and internal wave dynamics.

4. Discussion and Conclusions

4.1. Implications of Spatial and Temporal Scales and Resolution

Previous studies have emphasized the importance of topographic structures as habitats for sessile benthic fauna across various spatial dimensions. These topographic structures range from large-scale formations such as seamounts and large carbonate mounds at several tens of kilometers to smaller-scale features such as canyons and smaller carbonate mounds extending from hundreds of meters to a few kilometers at most (Iacono et al., 2018; Tittensor et al., 2009). With the widespread availability of detailed global bathymetric data, terrain attributes have been widely considered as useful predictor variables for ecological factors influencing the distribution of benthic fauna (Davies & Guinotte, 2011; Tong et al., 2023). Consequently, they are commonly utilized in modeling the distribution of benthic suspension feeder organisms particularly CWCs (Lecours et al., 2016; Miyamoto et al., 2017). However, only a limited number of studies have explored the significance of the spatial resolution of intricate topographic features in species distribution models and dynamic models of near-bottom currents. These studies have revealed a notable sensitivity of model predictions and flow-topography dynamics to the chosen spatial resolution of bathymetric data (e.g., Miyamoto et al., 2017; Mohn et al., 2013). In our model results of the central Valdivia Bank area, we also observe resolution-dependent variations in the physical descriptor variables across different model grids (Figures 11a and 11b). For example, although the coarser-resolution parent grid captures broader, large-scale lateral variations in kinetic energy dissipation rates (ε), employing a higher grid resolution and enhanced bathymetry in the child grid reveal finer-scale structures and variability (Figures 11a and
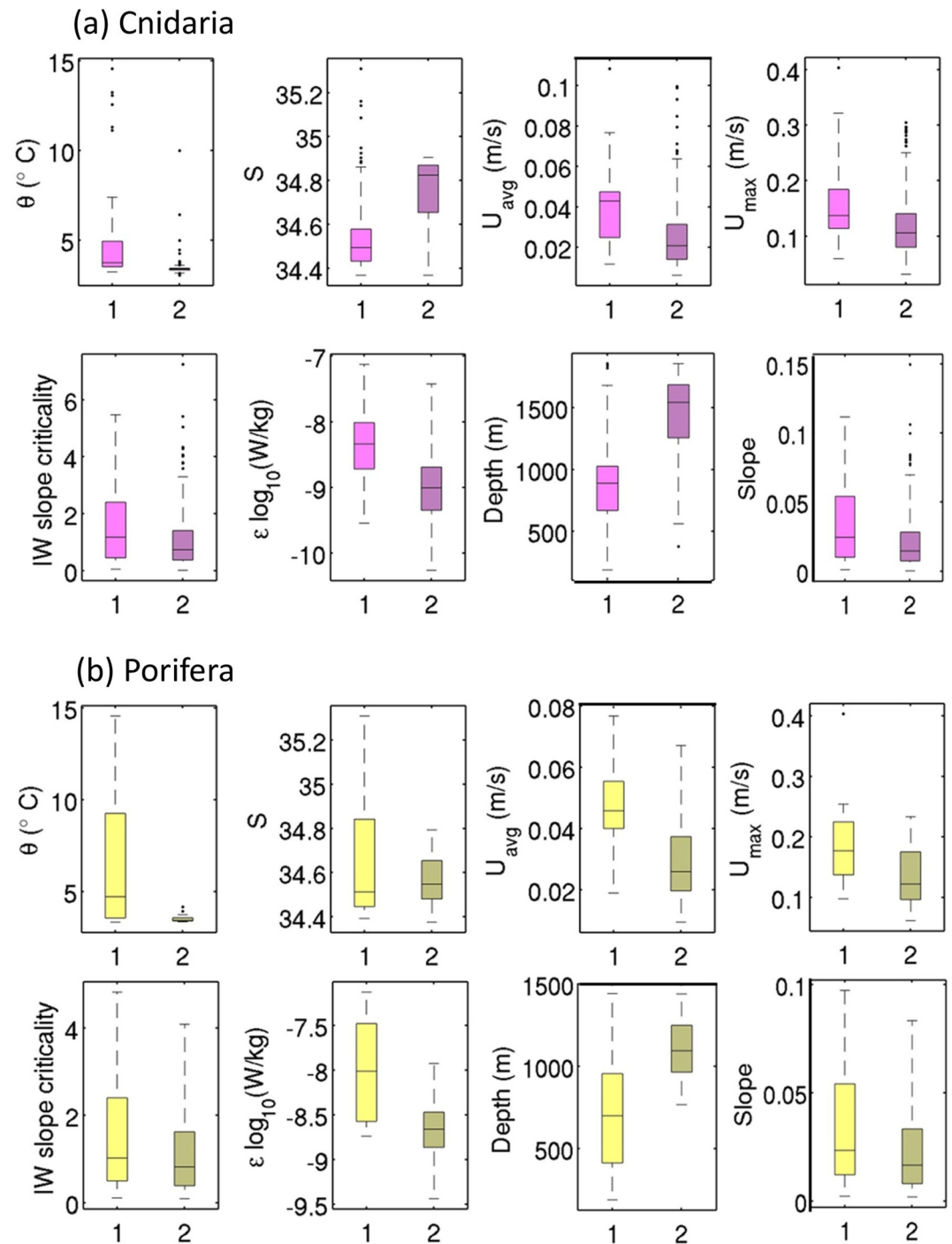
Figure 10. Box plots of near-bottom temperature θ (°C), salinity S, time-mean current speed U_{avg} (m s^{-1}), maximum current speed U_{max} (m s^{-1}), internal wave slope criticalit, kinetic energy dissipation $\log_{10}$ (ε) (W kg^{-1}), depth (m) and bottom slope for the two phyla Cnidaria (a) and Porifera (b) at observed presence (1) and randomly selected (pseudo) absence locations (2) at Valdivia Bank. Black horizontal bars represent the median. Colored boxes show the 25% and 75% quartiles. Whiskers extend two times the interquartile range indicating the spreading of values from minimum to maximum across the interquartile. The analysis is based on daily output from the 1,500 m resolution parent grid.

Kinetic energy dissipation – differences in spatial resolution
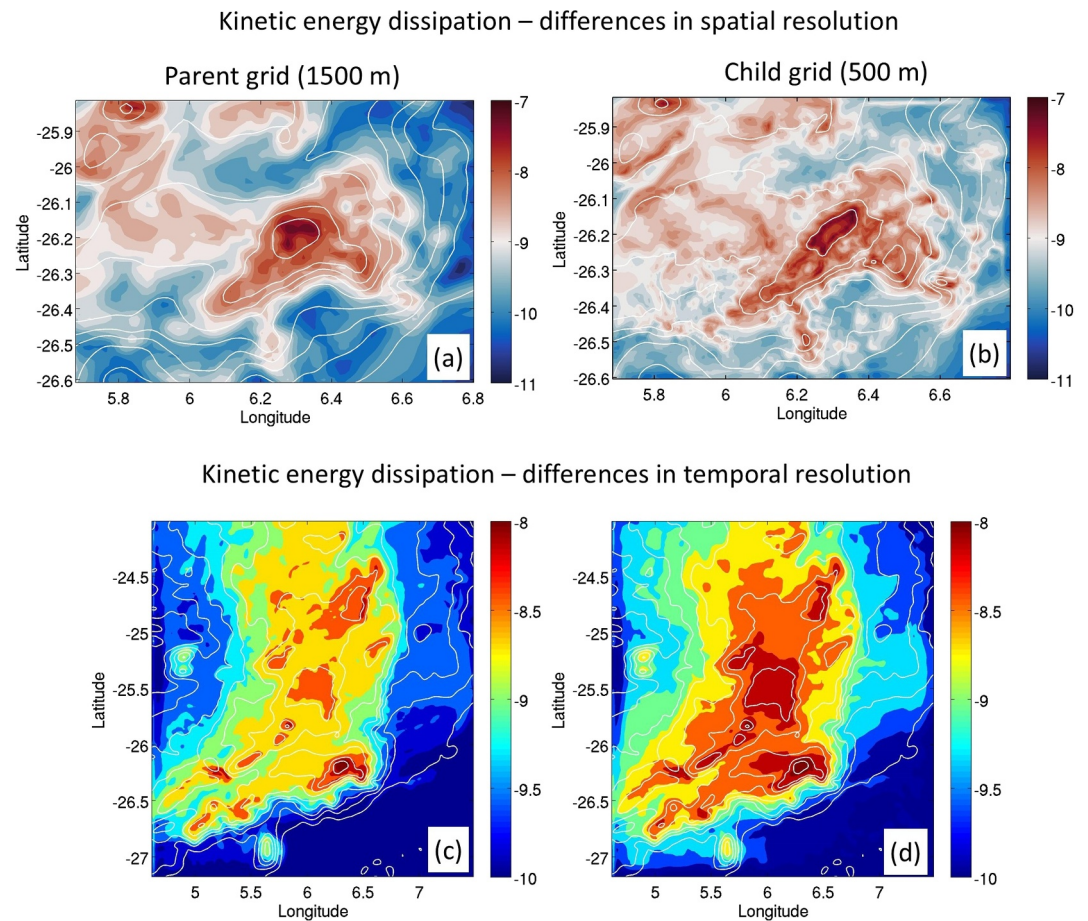
Figure 11. (a), (b) Mean near-bottom kinetic energy dissipation rate $\log_{10}(\varepsilon)$ (W kg^{-1}) and (c), (d) for different grid resolutions in the central Valdivia Bank model domain (c), (d) Mean near-bottom kinetic energy dissipation rates $\log10(\varepsilon)$ (W kg^{-1}) from 60 days of model simulations (parent grid; 1 January 2009, to 1 March 2009) calculated using daily averaged velocities (c) and 3-hourly instantaneous velocities (d).

11b). Consequently, resolution-dependent differences can also be anticipated for other functional environmental descriptors in regions with a complex terrain structure.

Our approach of incorporating physical processes as functional descriptors of predicting benthic suspension feeder assemblages also has conceptual limitations. We computed time-mean (long-term) averages of ε and S values to compare observed occurrences of Cnidaria and Porifera and randomly selected pseudo-absence locations with various dynamic environments. However, employing long-term averages of S may occasionally lead to misinterpretations. For instance, the internal wave slope criticality S delineates regimes with qualitatively distinct dynamics (ranging from subcritical to supercritical). If benthic suspension feeders tend to avoid the most turbulent environments, they might be present in environments with sub and supercritical slopes but absent in critical or near-critical slopes. Under such circumstances, computing time averages for S would yield values close to one (near-critical conditions), which would not accurately represent conditions typically attractive to these organisms. Additionally, we did not consider temporal variations on intra-day tidal, seasonal, and interannual timescales in internal wave slope criticality and kinetic energy dissipation. However, it has been demonstrated that seasonal changes in stratification can lead to significant changes in internal tide characteristics and dynamics (Cacchione et al., 2002). By using daily averaged current velocities and not accounting for excursions from intra-day tidal variations of the 3-D velocity field, the impact of tidal dynamics on the resulting shear of the velocity field and mean kinetic energy dissipation rates will likely be underestimated. Kinetic energy dissipation rates derived from 3-hourly instantaneous model output show increased dissipation rates over a larger area across the central Valdivia Bank compared to those derived from daily averaged data for the same simulation period (Figures 11c and

11d). We conclude that resolving the tidal cycle is likely to improve our understanding of the relationship between tidal dynamics and CWC distribution. This, in turn, would allow for a more accurate identification of areas where CWCs are likely to be present in relation to the physical conditions. In essence, long-term averages represent the necessary baseline conditions to estimate if the environment is broadly suitable and stable for growth, whereas resolving instantaneous conditions provide the dynamic context that directly influences feeding and, therefore, survival and growth rates on a shorter timescale (Cyr et al., 2016; Davies & Guinotte, 2011; Juva et al., 2020). Both are crucial for more accurate assessments of the persistence of these ecosystems and should be considered in future modeling efforts.

4.2. Benefits of Implementing Physical Processes for Predictions of Food Supply and Vulnerable Marine Ecosystem (VME) Indicator Species

Many cnidarians and sponges are VME indicator species, providing important ecosystem services (e.g., Bridges et al., 2021), forming in many cases Marine Animal Forests (MAFs) (Rossi et al., 2017) and have high conservation value (e.g., Armstrong et al., 2014). Yet, we still only have scattered knowledge about their global distribution and environmental drivers (Roberts & Cairns, 2014), and the South Atlantic is no exception (Bergstad, Gil, et al., 2019; Bridges, Howell, et al., 2023). An increasing number of benthic ecosystems dominated by cnidarians (particularly CWC species), and sponges have been extensively studied in recent years. This research has provided valuable data for local and basin-scale species distribution and habitat suitability models, significantly enhancing our understanding of the spatial occurrence and structure, temporal variability, and relationships with environmental variables of benthic filter-feeding deep-sea communities (Davies & Guinotte, 2011; Flögel et al., 2014; Knudby et al., 2013; Morato et al., 2020; Mosquera et al., 2019; Puerta et al., 2022; Sundahl et al., 2020). Observational and model studies have demonstrated that locally intensified hydrodynamics and high advection rates of food particles are important drivers for growth and well-being of CWCs (de Froe et al., 2022; Juva et al., 2020; Mienis et al., 2007; Soetaert et al., 2016). At such locations, kinetic energy is converted from large-scale currents and barotropic tides to internal tides creating locally enhanced turbulence and small-scale mixing over rough topography (Juva et al., 2020; Nikurashin et al., 2013). Alternatively, kinetic energy is advected from the oceanic far field through boundary currents carrying larvae and food (Schulz et al., 2020). Well-tested hydrodynamic models in combination with in situ sampling can resolve a large part of the spectrum of oceanic motions and thus can help to improve predictions of VME indicator species distribution at management scales of a few kilometers or less (e.g., Vinha et al., 2024). Dynamic downscaling resolves the 3-D velocity field at spatial scales that are relevant for larger cold water coral reefs and sponge assemblages in combination with high-resolution terrain data and accurate boundary conditions. Our model results from Valdivia Bank indicate that mechanistic descriptors calculated from modeled velocities and water mass properties can be useful proxies to supplement the more traditional predictors such as terrain variables and water mass properties in future species distribution modeling efforts. For example, enhanced kinetic energy dissipation rates and areas of internal wave generation and propagation appear to be closely linked to benthic fauna occurrence. Although our model is limited in its ability to resolve fine-scale or highly dynamic ocean processes and does not explicitly capture nonlinear processes such as turbulence and internal wave breaking, it can still provide valuable mechanistic proxies, such as estimates of kinetic energy dissipation and internal wave characteristics that can act as indicators of areas where enhanced vertical mixing might occur. These proxies are useful in species distribution models, allowing us to identify potential hotspots of particle flux and areas likely to support benthic filter feeders. Insights gained from our model could potentially be upscaled to other regions with similar environmental, topographic, and ecological conditions. Although local models are tuned to capture site-specific dynamics, the functional relationships they predict can inform broader regionally scaled or even basin-wide evaluations and contribute to a comparative modeling framework.

Data Availability Statement

The CTD data used for model validation are available at the IEO marine geospatial information Walvis Ridge viewer open repository (https://www.ieo.es/es/ideo). The benthos data from the Spanish-Namibian surveys are available from the Ocean Biodiversity Information System (OBIS) at https://www.gbif.org/dataset/c3fa13f7-14bd-4f14-9bd5-4f959860f63b. The ROMS-AGRIF model used in this study is now frozen and replaced by the CROCO project (https://www.croco-ocean.org/history/). The CROCO model includes all the functionalities of

ROMS_AGRIF and added additional features (e.g., non-hydrostatic kernel). The tidal forcing data (OTIS-TPXO) and atmospheric forcing data (COADS) can be downloaded from https://www.croco-ocean.org/download/.

References

Armstrong, C. W., Foley, N. S., Kahui, V., & Grehan, A. (2014). Cold water coral reef management from an ecosystem service perspective. *Marine Policy*, *50*, 126–134. https://doi.org/10.1016/j.marpol.2014.05.016

Barbet-Massin, M., Jiguet, F., Albert, C. H., & Thuiller, W. (2012). Selecting pseudo-absences for species distribution models: How, where and how many? *Methods in Ecology and Evolution*, *3*(2), 327–338. https://doi.org/10.1111/j.2041-210X.2011.00172.x

Bashmachnikov, I., Mohn, C., Pelegrí, J. L., Martins, A., Jose, F., Machín, F., & White, M. (2009). Interaction of Mediterranean water eddies with Sedlo and seine seamounts, subtropical northeast Atlantic. *Deep Sea Research Part II: Topical Studies in Oceanography*, *56*(25), 2593–2605. https://doi.org/10.1016/j.dsr2.2008.12.036

Bergstad, O. A., Gil, M., Høines, Å. S., Sarralde, R., Maletzky, E., Mostarda, E., et al. (2019). Megabenthos and benthopelagic fishes on Southeast Atlantic seamounts. *African Journal of Marine Science*, *41*(1), 29–50. https://doi.org/10.2989/1814232X.2019.1571439

Bergstad, O. A., Høines, Å. S., Sarralde, R., Campanis, G., Gil, M., Ramil, F., et al. (2019). Bathymetry, substrate and fishing areas of Southeast Atlantic high-seas seamounts. *African Journal of Marine Science*, *41*(1), 11–28. https://doi.org/10.2989/1814232x.2019.1569160

Bridges, A. E., Barnes, D. K., Bell, J. B., Ross, R. E., Voges, L., & Howell, K. L. (2023). Filling the data gaps: Transferring models from data-rich to data-poor deep-sea areas to support spatial management. *Journal of Environmental Management*, *345*, 118325. https://doi.org/10.1016/j.jenvman.2023.118325

Bridges, A. E., Howell, K. L., Amaro, T., Atkinson, L., Barnes, D. K. A., Bax, N., et al. (2023). Review of the central and south Atlantic shelf and deep-sea benthos: Science, policy, and management. *Oceanography and Marine Biology an Annual Review*, *61*, 127–218. https://doi.org/10.1201/9781003363873-5

Bridges, A. E. H., Barnes, D. K. A., Bell, J. B., Ross, R. E., & Howell, K. L. (2021). Benthic assemblage composition of South Atlantic seamounts. *Frontiers in Marine Science*, *8*. https://doi.org/10.3389/fmars.2021.660648

Cacchione, D. A., Pratson, L. F., & Ogston, A. S. (2002). The shaping of continental slopes by internal tides. *Science*, *296*(5568), 724–727. https://doi.org/10.1126/science.1069803

Casanova-Masjoan, M., Pelegrí, J. L., Sangrà, P., Martínez, A., Grisolía-Santos, D., Pérez-Hernández, M. D., & Hernández-Guerra, A. (2017). Characteristics and evolution of an Agulhas ring. *Journal of Geophysical Research: Oceans*, *122*(9), 7049–7065. https://doi.org/10.1002/2017JC012969

Chelton, D. B., Schlax, M. G., & Samelson, R. M. (2011). Global observations of nonlinear mesoscale eddies. *Progress in Oceanography*, *91*(2), 167–216. https://doi.org/10.1016/j.pocean.2011.01.002

Chidichimo, M. P., Perez, R. C., Speich, S., Kersalé, M., Sprintall, J., Dong, S., et al. (2023). Energetic overturning flows, dynamic interocean exchanges, and ocean warming observed in the South Atlantic. *Communications Earth & Environment*, *4*(1), 10. https://doi.org/10.1038/s43247-022-00644-x

Contreras, E., Jiménez García, P., Sager, W. W., Thoram, S., Hoernle, K., Sarralde, R., & Zhou, H. (2022). Bathymetry of Valdivia Bank, Walvis Ridge, South Atlantic ocean: 2 implications for structure and geologic history of a hot spot plateau. *Geochemistry, Geophysics, Geosystems*, *23*(11). https://doi.org/10.1029/2022GC010624

Cyr, F., van Haren, H., Mienis, F., Duineveld, G., & Bourgault, D. (2016). On the influence of cold-water coral mound size on flow hydrodynamics, and vice versa. *Geophysical Research Letters*, *43*(2), 775–783. https://doi.org/10.1002/2015gl067038

Davies, A. J., & Guinotte, J. M. (2011). Global habitat suitability for framework-forming cold-water corals. *PLoS One*, *6*(4), e18483. https://doi.org/10.1371/journal.pone.0018483

De Froe, E., Maier, S. R., Horn, H. G., Wolff, G. A., Blackbird, S., Mohn, C., et al. (2022). Hydrography and food distribution during a tidal cycle above a cold-water coral mound. *Deep Sea Research Part I: Oceanographic Research Papers*, *189*, 103854. https://doi.org/10.1016/j.dsr.2022.103854

Dencausse, G., Arhan, M., & Speich, S. (2010). Routes of Agulhas rings in the southeastern Cape Basin. *Deep Sea Research Part I: Oceanographic Research Papers*, *57*(11), 1406–1421. https://doi.org/10.1016/j.dsr.2010.07.008

Drazen, J. C., Lisa, G., & Domokos, R. (2011). Micronekton abundance and biomass in Hawaiian waters as influenced by seamounts, eddies, and the moon. *Deep Sea Research Part I: Oceanographic Research Papers*, *58*(5), 557–566. https://doi.org/10.1016/j.dsr.2011.03.002

Durán Muñoz, P., Sayago-Gil, M., Murillo, F. J., Del Río, J. L., López-Abellán, L. J., Sacau, M., & Sarralde, R. (2012). Actions taken by fishing nations towards identification and protection of vulnerable marine ecosystems in the high seas: The Spanish case (Atlantic Ocean). *Marine Policy*, *36*(2), 536–543. https://doi.org/10.1016/j.marpol.2011.09.005

Egbert, G. D., & Erofeeva, S. Y. (2002). Efficient inverse modeling of barotropic ocean tides. *Journal of Atmospheric and Oceanic Technology*, *19*(2), 183–204. https://doi.org/10.1175/1520-0426(2002)019%3C0183:EIMOBO%3E2.0.CO;2

FAO (2009). International Guidelines for the Management of Deep-sea Fisheries in the High Seas. Directives internationales sur la gestion de la p che profonde en haute mer. *Directrices Internacionales para la Ordenaci n de las Pesquer as de Aguas Profundas en Alta Mar. Rome/ Roma*, 73.

Flögel, S., Dullo, W.-C., Pfannkuche, O., Kiriakoulakis, K., & Rüggeberg, A. (2014). Geochemical and physical constraints for the occurrence of living cold-water corals. *Deep Sea Research Part II: Topical Studies in Oceanography*, *99*, 19–26. https://doi.org/10.1016/j.dsr2.2013.06.006

Gevorgian, J., Sandwell, D. T., Yu, Y., Kim, S. S., & Wessel, P. (2023). Global distribution and morphology of small seamounts. *Earth and Space Science*, *10*(4), e2022EA002331. https://doi.org/10.1029/2022EA002331

Giacomello, E., Menezes, G. M., & Bergstad, O. A. (2013). An integrated approach for studying seamounts: CONDOR observatory. *Deep-Sea Research Part II*, *98*(98), 1–6. https://doi.org/10.1016/j.dsr2.2013.09.023

Haidvogel, D. B., Beckmann, A., Chapman, D. C., & Lin, R. Q. (1993). Numerical simulation of flow around a tall isolated seamount. Part II: Resonant generation of trapped waves. *Journal of Physical Oceanography*, *23*(11), 2373–2391. https://doi.org/10.1175/1520-0485(1993)023<2373:nsofaa>2.0.co;2

Iacono, C. L., Robert, K., Gonzalez-Villanueva, R., Gori, A., Gili, J. M., & Orejas, C. (2018). Predicting cold-water coral distribution in the Cap de Creus Canyon (NW Mediterranean): Implications for marine conservation planning. *Progress in Oceanography*, *169*, 169–180. https://doi.org/10.1016/j.pocean.2018.02.012

Juva, K., Flögel, S., Karstensen, J., Linke, P., & Dullo, W.-C. (2020). Tidal dynamics control on cold-water coral growth: A high-resolution multivariable study on eastern Atlantic cold-water coral sites. *Frontiers in Marine Science*, *7*, 132. https://doi.org/10.3389/fmars.2020.00132

Khripounoff, A., Caprais, J. C., Le Bruchec, J., Rodier, P., Noel, P., & Cathalot, C. (2014). Deep cold-water coral ecosystems in the Brittany submarine canyons (Northeast Atlantic): Hydrodynamics, particle supply, respiration, and carbon cycling. *Limnology & Oceanography*, *59*(1), 87–98. https://doi.org/10.4319/lo.2014.59.1.0087

Knudby, A., Kenchington, E., & Murillo, F. J. (2013). Modeling the distribution of Geodia sponges and sponge grounds in the Northwest Atlantic. *PLoS One*, *8*(12), e82306. https://doi.org/10.1371/journal.pone.0082306

Kunze, E., & Toole, J. M. (1997). Tidally driven vorticity, diurnal shear, and turbulence atop Fieberling Seamount. *Journal of Physical Oceanography*, *27*(12), 2663–2693. https://doi.org/10.1175/1520-0485(1997)027<2663:tdvdsa>2.0.co;2

Lavelle, J. W., & Mohn, C. (2010). Motion, commotion, and biophysical connections at deep ocean seamounts. *Oceanography*, *23*(1), 90–103. https://doi.org/10.5670/oceanog.2010.64

Lecours, V., Brown, C. J., Devillers, R., Lucieer, V. L., & Edinger, E. N. (2016). Comparing selections of environmental variables for ecological studies: A focus on terrain attributes. *PLoS One*, *11*(12), e0167128. https://doi.org/10.1371/journal.pone.0167128

Liu, M., & Tanhua, T. (2021). Water masses in the Atlantic Ocean: Characteristics and distributions. *Ocean Science*, *17*(2), 463–486. https://doi.org/10.5194/os-17-463-2021

López-Abellán, L. J., & Holtzhausen, H. (2011). *Preliminary report of the multidisciplinary research cruise on the Walvis Ridge seamounts (Atlantic Southeast, SEAFO)*. National Marine Information and Research Centre.

Maier, S. R., Brooke, S., De Clippele, L. H., de Foe, E., van der Kaaden, A. S., Kutti, T., et al. (2023). On the paradox of thriving cold-water coral reefs in the food-limited deep sea. *Biological Reviews*, *98*(5), 1768–1795. https://doi.org/10.1111/brv.12976

Maldonado, M., Aguilar, R., Bannister, R. J., Bell, J. J., Conway, K. W., Dayton, P. K., et al. (2017). Sponge grounds as key marine habitats: A synthetic review of types, structure, functional roles, and conservation concerns. In S. Rossi, L. Bramanti, A. Gori, & C. Orejas (Eds.), *Marine animal forests* (pp. 145–184). Springer. https://doi.org/10.1007/978-3-319-21012-4_24

McQuaid, K. A., Bridges, A. E., Howell, K. L., Gandra, T. B., de Souza, V., Currie, J. C., et al. (2023). Broad-scale benthic habitat classification of the South Atlantic. *Progress in Oceanography*, *214*, 103016. https://doi.org/10.1016/j.pocean.2023.103016

Mienis, F., De Stigter, H. C., White, M., Duineveld, G., De Haas, H., & Van Weering, T. C. E. (2007). Hydrodynamic controls on cold-water coral growth and carbonate-mound development at the SW and SE Rockall Trough Margin, NE Atlantic Ocean. *Deep Sea Research Part I: Oceanographic Research Papers*, *54*(9), 1655–1674. https://doi.org/10.1016/j.dsr.2007.05.013

Miyamoto, M., Kiyota, M., Murase, H., Nakamura, T., & Hayashibara, T. (2017). Effects of bathymetric grid-cell sizes on habitat suitability analysis of cold-water Gorgonian corals on seamounts. *Marine Geodesy*, *40*(4), 205–223. https://doi.org/10.1080/01490419.2017.1315543

Mohn, C., Erofeeva, S., Turnewitsch, R., Christiansen, B., & White, M. (2013). Tidal and residual currents over abrupt deep-sea topography based on shipboard ADCP data and tidal model solutions for three popular bathymetry grids. *Ocean Dynamics*, *63*(2–3), 195–208. https://doi.org/10.1007/s10236-013-0597-1

Mohn, C., Hansen, J. L., Carreiro-Silva, M., Cunningham, S. A., de Froe, E., Dominguez-Carrió, C., et al. (2023). Tidal to decadal scale hydrodynamics at two contrasting cold-water coral sites in the Northeast Atlantic. *Progress in Oceanography*, *214*, 103031. https://doi.org/10.1016/j.pocean.2023.103031

Mohrholz, V., Eggert, A., Junker, T., Nausch, G., Ohde, T., & Schmidt, M. (2014). Cross shelf hydrographic and hydrochemical conditions and their short-term variability at the northern Benguela during a normal upwelling season. *Journal of Marine Systems*, *140*, 92–110. https://doi.org/10.1016/j.jmarsys.2014.04.019

Morato, T., González-Irusta, J.-M., Dominguez-Carrió, C., Wei, C.-L., Davies, A., Sweetman, A. K., et al. (2020). Climate-induced changes in the suitable habitat of cold-water corals and commercially important deep-sea fishes in the North Atlantic. *Global Change Biology*, *26*(4), 2181–2202. https://doi.org/10.1111/gcb.14996

Mosquera Giménez, Á., Vélez-Belchí, P., Rivera, J., Piñeiro, S., Fajar, N., Caínzos, V., et al. (2019). Ocean circulation over North Atlantic underwater features in the path of the Mediterranean Outflow Water: The Ormonde and Formigas seamounts, and the Gazul Mud volcano. *Frontiers in Marine Science*, *6*, 702. https://doi.org/10.3389/fmars.2019.00702

Nikurashin, M., Vallis, G. K., & Adcroft, A. (2013). Routes to energy dissipation for geostrophic flows in the Southern Ocean. *Nature Geoscience*, *6*(1), 48–51. https://doi.org/10.1038/ngeo1657

Orejas, C., Carreiro-Silva, M., Mohn, C., Reimer, J. D., Samaai, T., Allcock, A. L., & Rossi, S. (2022). Marine Animal Forests of the World: Definition and Characteristics. Research Ideas and Outcomes. *Research Ideas and Outcomes*, *8*. https://doi.org/10.3897/rio.8.e96274

Orejas, C., & Jimenez, C. (2017). The Builders of the oceans – Part I: Coral architecture from the tropics to the Poles, from the shallow to the deep. In S. Rossi, L. Bramanti, A. Gori, & C. Orejas (Eds.), *Marine animal forests marine animal forests* (pp. 627–655). Springer. https://doi.org/10.1007/978-3-319-21012-4_10

Pearman, T. R., Robert, K., Callaway, A., Hall, R. A., Mienis, F., & Huvenne, V. A. (2023). Spatial and temporal environmental heterogeneity induced by internal tides influences faunal patterns on vertical walls within a submarine canyon. *Frontiers in Marine Science*, *10*, 1091855. https://doi.org/10.3389/fmars.2023.1091855

Puerta, P., Mosquera-Giménez, Á., Renones, O., Domínguez-Carrió, C., Rueda, J. L., Urra, J., et al. (2022). Variability of deep-sea megabenthic assemblages along the western pathway of the Mediterranean outflow water. *Deep Sea Research Part I: Oceanographic Research Papers*, *185*, 103791. https://doi.org/10.1016/j.dsr.2022.103791

Ramiro-Sánchez, B., González-Irusta, J. M., Henry, L. A., Cleland, J., Yeo, I., Xavier, J. R., et al. (2019). Characterization and mapping of a deep-sea sponge ground on the tropic seamount (northeast tropical Atlantic): Implications for spatial management in the high seas. *Frontiers in Marine Science*, *6*. https://doi.org/10.3389/fmars.2019.00278

Roberts, J. M., & Cairns, S. D. (2014). Cold-water corals in a changing ocean. *Current Opinion in Environmental Sustainability*, *7*, 118–126. https://doi.org/10.1016/j.cosust.2014.01.004

Roberts, J. M., Wheeler, A. J., & Freiwald, A. (2006). Reefs of the deep: The biology and geology of cold-water coral ecosystems. *Science*, *312*(5773), 543–547. https://doi.org/10.1126/science.1119861

Rogers, A. D. (2018). The biology of seamounts: 25 years on. *Advances in Marine Biology*, *79*, 137–224. https://doi.org/10.1016/bs.amb.2018.06.001

Rossi, S., Bramanti, L., Gori, A., & Orejas, C. (2017). *The ecology of benthic biodiversity hotspots* (p. 1369). Springer. https://doi.org/10.1007/978-3-319-21012-4

Rühs, S., Schmidt, C., Schubert, R., Schulzki, T. G., Schwarzkopf, F. U., Le Bars, D., & Biastoch, A. (2022). Robust estimates for the decadal evolution of Agulhas leakage from the 1960s to the 2010s. *Communications Earth & Environment*, *3*(1), 318. https://doi.org/10.1038/s43247-022-00643-y

Rühs, S., Schwarzkopf, F. U., Speich, S., & Biastoch, A. (2019). Cold vs. warm water route – Sources for the upper limb of the Atlantic Meridional Overturning Circulation revisited in a high-resolution ocean model. *Ocean Science*, *15*(3), 489–512. https://doi.org/10.5194/os-15-489-2019

Schouten, M. W., de Ruijter, W. P., Van Leeuwen, P. J., & Lutjeharms, J. R. (2000). Translation, decay and splitting of Agulhas rings in the southeastern Atlantic Ocean. *Journal of Geophysical Research*, *105*(C9), 21913–21925. https://doi.org/10.1029/1999jc000046

Schulz, K., Soetaert, K., Mohn, C., Korte, L., Mienis, F., Duineveld, G., & van Oevelen, D. (2020). Linking large-scale circulation patterns to the distribution of cold water corals along the eastern Rockall Bank (northeast Atlantic). *Journal of Marine Systems*, *212*, 103456. https://doi.org/10.1016/j.jmarsys.2020.103456

Schumacher, M., Huvenne, V. A. I., Devey, C. W., Arbizu, P. M., Biastoch, A., & Meinecke, S. (2022). The Atlantic Ocean landscape: A basin-wide cluster analysis of the Atlantic near seafloor environment. *Frontiers in Marine Science*, *9*. https://doi.org/10.3389/fmars.2022.936095

Schwarzkopf, F. U., Biastoch, A., Böning, C. W., Chanut, J., Durgadoo, J. V., Getzlaff, K., et al. (2019). The INALT family–a set of high-resolution nests for the Agulhas Current system within global NEMO ocean/sea-ice configurations. *Geoscientific Model Development*, *12*(7), 3329–3355. https://doi.org/10.5194/gmd-12-3329-2019

SEAFO. (2019). Dr Fridtjof Nansen survey 2019 – Cruise report. *SEAFO 15th Scientific Committee Meeting. DOC/SC/05/2019. Swakopmund, Namibia*.

SEAFO. (2022). Dr Fridtjof Nansen survey 2022 – Cruise report. *SEAFO 18th Scientific Committee Meeting. DOC/SC/03/2022. Swakopmund, Namibia*.

Serrano, A., González-Irusta, J. M., Punzón, A., García-Alegre, A., Lourido, A., Ríos, P., et al. (2017). Deep-sea benthic habitats modeling and mapping in a NE Atlantic seamount (Galicia Bank). *Deep-Sea Research*, *I*, 115–127. https://doi.org/10.1016/j.dsr.2017.06.003

Shapiro, G. I., Meschanov, S. L., & Emelianov, M. V. (1995). Mediterranean lens Irving after its collision with seamounts. *Oceanologica Acta*, *18*(3), 309–318. Retrieved from https://archimer.ifremer.fr/doc/00097/20780/

Shchepetkin, A. F., & McWilliams, J. C. (2005). The regional oceanic modeling system (ROMS): A split-explicit, free-surface, topography-following-coordinate oceanic model. *Ocean Modelling*, *9*(4), 347–404. https://doi.org/10.1016/j.ocemod.2004.08.002

Simpson, A., & Watling, L. (2011). Precious corals (Coralliidae) from north-western Atlantic seamounts. *Journal of the Marine Biological Association of the United Kingdom*, *91*(2), 369–382. https://doi.org/10.1017/s002531541000086x

Soetaert, K., Mohn, C., Rengstorf, A., Grehan, A., & van Oevelen, D. (2016). Ecosystem engineering creates a direct nutritional link between 600-m deep cold-water coral mounds and surface productivity. *Scientific Reports*, *6*(1), 35057. https://doi.org/10.1038/srep35057

St. Laurent, L., & Garrett, C. (2002). The role of internal tides in mixing the deep ocean. *Journal of Physical Oceanography*, *32*(10), 2882–2899. https://doi.org/10.1175/1520-0485(2002)032%3C2882:TROITI%3E2.0.CO;2

Stramma, L., & England, M. H. (1999). On the water masses and mean circulation of the South Atlantic Ocean. *Journal of Geophysical Research*, *104*(C9), 20863–20883. https://doi.org/10.1029/1999JC900139

Sundahl, H., Buhl-Mortensen, P., & Buhl-Mortensen, L. (2020). Distribution and suitable habitat of the cold-water corals Lophelia pertusa, Paragorgia arborea, and Primnoa resedaeformis on the Norwegian continental shelf. *Frontiers in Marine Science*, *7*, 213. https://doi.org/10.3389/fmars.2020.00213

Thorpe, S. A. (2007). *An introduction to ocean turbulence*. Cambridge University Press. https://doi.org/10.1017/CBO9780511801198

Tim, N., Zorita, E., Schwarzkopf, F. U., Rühs, S., Emeis, K.-C., & Biastoch, A. (2018). The impact of Agulhas leakage on the central water masses in the Benguela upwelling system from a high-resolution ocean simulation. *Journal of Geophysical Research: Oceans*, *123*(12), 9416–9428. https://doi.org/10.1029/2018JC014218

Tittensor, D. P., Baco, A. R., Brewin, P. E., Clark, M. R., Consalvey, M., Hall-Spencer, J., et al. (2009). Predicting global habitat suitability for stony corals on seamounts. *Journal of Biogeography*, *36*(6), 1111–1128. https://doi.org/10.1111/j.1365-2699.2008.02062.x

Tojeira, I., Pinto-Ribeiro, L., Rafael, T., Albuquerque, M., Simoes, M., Calado, A., et al. (2023). Preliminary deep-sea data analysis collected at Gloria seamount, Azores-Biscay Rise. *Continental Shelf Research*, *267*, 105100. https://doi.org/10.1016/j.csr.2023.105100

Tong, R., Davies, A. J., Yesson, C., Yu, J., Luo, Y., Zhang, L., & Burgos, J. M. (2023). Environmental drivers and the distribution of cold-water corals in the global ocean. *Frontiers in Marine Science*, *10*, 1217851. https://doi.org/10.3389/fmars.2023.1217851

Tsujino, H., Urakawa, L. S., Griffies, S. M., Danabasoglu, G., Adcroft, A. J., Amaral, A. E., et al. (2020). Evaluation of global ocean–sea-ice model simulations based on the experimental protocols of the Ocean Model Intercomparison Project phase 2 (OMIP-2). *Geoscientific Model Development*, *13*(8), 3643–3708. https://doi.org/10.5194/gmd-13-3643-2020

Tsujino, H., Urakawa, S., Nakano, H., Small, R. J., Kim, W. M., Yeager, S. G., et al. (2018). JRA-55 based surface dataset for driving ocean–sea-ice models (JRA55-do). *Ocean Modelling*, *130*, 79–139. https://doi.org/10.1016/j.ocemod.2018.07.002

Van der Kaaden, A. S., Mohn, C., Gerkema, T., Maier, S. R., de Froe, E., van de Koppel, J., et al. (2021). Feedbacks between hydrodynamics and cold-water coral mound development. *Deep Sea Research Part I: Oceanographic Research Papers*, *178*, 103641. https://doi.org/10.1016/j.dsr.2021.10364

van Heuven, S. M. A. C., Hoppema, M., Huhn, O., Slagter, H. A., & de Baar, H. J. W. (2011). Direct observation of increasing CO2 in the Weddell Gyre along the Prime Meridian during 1973–2008. *Deep-Sea Research*, *58*(25–26), 2613–2635. https://doi.org/10.1016/j.dsr2.2011.08.007

Vinha, B., Murillo, F. J., Schumacher, M., Hansteen, T. H., Schwarzkopf, F. U., Biastoch, A., et al. (2024). Ensemble modelling to predict the distribution of vulnerable marine ecosystems indicator taxa on data-limited seamounts of Cabo Verde (NW Africa). *Diversity and Distributions*, *30*(8), e13896. https://doi.org/10.1111/ddi.13896

Vlasenko, V., Stashchuk, N., & Nimmo-Smith, W. A. M. (2018). Three-dimensional dynamics of baroclinic tides over a seamount. *Journal of Geophysical Research: Oceans*, *123*(2), 1263–1285. https://doi.org/10.1002/2017jc013287

Wessel, P., Sandwell, D. T., & Kim, S. S. (2010). The global seamount census. *Oceanography*, *23*(1), 24–33. https://doi.org/10.5670/oceanog.2010.60